Structural and Functional Insights into the Action Mode of A Mitochondrial AAA+ Disaggregase CLPB

Damu Wu[1], Yan Liu[2], Yuhao Dai[1,3], Guopeng Wang[1], Guoliang Lu[2], Yan Chen[1], Ningning Li[1], Jinzhong Lin[2,*], Ning Gao[1,*]

[1]State Key Laboratory of Membrane Biology, Peking-Tsinghua Joint Center for Life Sciences, School of Life Sciences, Peking University, Beijing 100871, China.

[2]State Key Laboratory of Genetic Engineering, School of Life Sciences, Zhongshan Hospital, Fudan University, Shanghai 200438, China

[3]Academy of Advanced Interdisciplinary Studies, Peking University, Beijing 100871, China.

*Correspondence to: gaon@pku.edu.cn (N.G.); linjinzhong@fudan.edu.cn (J.L.)

Abstract

The human AAA+ ATPase CLPB (SKD3) is a protein disaggregase in the mitochondrial intermembrane space and functions to promote the solubilization of various mitochondrial proteins. CLPB deficiency by mutations is associated with a few human diseases with neutropenia and neurological disorders. Unlike canonical AAA+ proteins, CLPB contains a unique ankyrin repeat domain (ANK) at its N-terminus. The mechanism of CLPB functions as a disaggregase and the role of its ANK domain are currently unclear. Herein, we report a comprehensive structural characterization of human CLPB in both the apo- and substrate-bound states. CLPB assembles into homo-tetradecamers in apo-state and is remodeled into homo-dodecamers upon binding to substrates. Conserved pore-loops on the ATPase domains form a spiral staircase to grip and translocate the substrate in a step-size of two amino acid residues. The ANK domain is not only responsible for maintaining the higher-order assembly but also essential for the disaggregase activity. Interactome analysis suggests that the ANK domain may directly interact with a variety of mitochondrial substrates. These results reveal unique properties of CLPB as a general disaggregase in mitochondria and highlight its potential as a target for the treatment of various mitochondria-related diseases.

Introduction

Protein misfolding and aberrant aggregation are devastating to many fundamental functions of the cell and failures to remediate them are closed related to many human diseases (Eisele et al., 2015; Soto and Pritzkow, 2018). To maintain a healthy proteome, cells have evolved multiple dedicated systems, one of which is the HSP100 chaperone family (Erzberger and Berger, 2006; Kirstein et al., 2009; Puchades et al., 2020). As a subfamily of the AAA+ ATPase, HSP100 proteins generally contain an N-terminal domain (NTD), one or two ATPase domains (or nucleotide-binding domain, NBD), and usually function in hexameric forms. Taking yeast Hsp104 as an example, the NTD is involved in substrate binding, while the NBD1 and NBD2 bind and hydrolyze ATP to facilitate power substrate unfolding and translocation (Grimminger-Marquardt and Lashuel, 2010). Similar to many other AAA+ ATPases, Hsp104 unfolds and transports substrates through its central pore by a ratchet-like motion of the highly conserved pore-loops (PL) on the ATPase domains (Gates et al., 2017). The ATP-hydrolysis cycle dependent conformational change of each subunit results in both inter- and intra-subunit structural remodeling, which collectively lead to the threading and unidirectional movement of the peptide within the central channel (Gates et al., 2017).

Recently, a new type of HSP100 family proteins, CLPB (also known as SKD3) was reported to act as a protein disaggregase in the intermembrane space (IMS) of mitochondria (Cupo and Shorter, 2020; Mroz et al., 2020; Thevarajan et al., 2020; Wortmann et al., 2015). The N-terminus of CLPB has a mitochondrial targeting signal (MTS), followed by an ankyrin repeat (ANK) domain, and ends with a C-terminal NBD (Fig. 1A). There is a short hydrophobic stretch between the MTS and the first ankyrin motif, as well as a long linker helix (LH) between ANK domain and NBD (Fig. 1A). The MTS is cleaved by mitochondrial processing peptidase (MPP), followed by a second cleavage by presenilin-associated rhomboid-like (PARL) protease to remove additional hydrophobic residues from the N-terminus (Saita et al., 2017; Thevarajan et al., 2020). The ANK domain is a unique feature of CLPB compared to other AAA+ ATPases, and the removal of ANK domain disrupts the disaggregase activity of CLPB (Cupo and Shorter, 2020).

Dysfunction of CLPB by mutations are associated with several human diseases, such as the 3-methylglutaconic aciduria (3-MGA) (Capo-Chichi et al., 2015; Kanabus et al., 2015; Kiykim et al., 2016; Saunders et al., 2015; Wortmann et al., 2015). A common disorder of the 3-MGA patients is the increased urinary 3-methylglutaric acid excretion, often with varying degree of microcephaly, small birth weight, neutropenia, severe encephalopathy,

intellectual disability, movement disorder and cataracts (Capo-Chichi et al., 2015; Kanabus et al., 2015; Kiykim et al., 2016; Saunders et al., 2015; Wortmann et al., 2015). Moreover, heterozygous missense variants of CLPB were also identified in patients with severe congenital neutropenia (SCN), and these variants were found to disrupt granulocyte differentiation of human hematopoietic progenitors (Warren et al., 2022). Many of these disease-related mutations have been shown to impair the disaggregase activity of CLPB, such as T268M, R408G, R475Q, A591V, R650P in 3-MGA and N499K, E557K, R561G, R620C in SCN (Cupo and Shorter, 2020; Warren et al., 2022). At the cellular level, CLPB is important in maintaining normal cristae structure of mitochondria (Chen et al., 2019b). CLPB interacts with HAX1, an anti-apoptotic factor of BCL-2 family, to promote cell survival (Chen et al., 2019b; Wortmann et al., 2015). Upregulated cellular level of CLPB in acute myeloid leukemia (AML) cells was found to mediate the resistance to BCL-2 inhibitor venetoclax (Chen et al., 2019b). Recently, CLPB was also found to have negative correlation with the progression-free survival in castration-resistant prostate cancer (Pudova et al., 2020).

It is currently not clear why CLPB has such a broad role in different aspects of mitochondrial function, and how the ANK and NBD domains work together to fulfil its essential disaggregase activity. Here, we present a structural and functional characterization of human CLPB. Unexpectedly, we found that CLPB assembles into a homo-tetradecamers in the absence of substrate. Upon substrate binding, the CLPB complex is converted into dodecamers consisting two conventional hexameric units. The NBD ring within a hexamer shares common structural features of typical AAA+ unfoldase/disaggreagase, with a spiral arrangement of pore-loops to interact with a fully threaded substrate. The N-terminal ANK domain is essential for the higher-order organization of CLPB, and contributes to the disggregase activity by directly interacting with various mitochondrial substrates. These results provide a framework for further dissection of the role of CLPB in regulating mitochondrial functions.

Results

Cryo-EM structures of CLPB in the apo-state and substrate-bound state

We cloned the coding sequence of *CLPB* from a home-made cDNA library of HEK-293T cells, and sequencing result indicated that it was the splicing isoform 2 (UNIPROT: Q9H078-2). Different expression constructs were tested. Firstly, CLPB without the mitochondrial targeting sequence (MTS) (Wortmann et al., 2015), named CLPB-N92 (Fig. 1A), was expressed and purified from *E. coli* cells. Consistent with a previous study (Mroz et al., 2020), CLPB-N92 formed large aggregates and was highly heterogenous in size as shown by gel filtration and negative-

staining electron microscopy (nsEM) (Supplementary Fig. 1A and B). In addition to the signal peptide removal, CLPB was reported to be further processed by a mitochondrial protease PARL localized in the inner membrane, and the predicted cleavage site is between C126 and Y127 (Saita et al., 2017). Notably, a hydrophobic stretch within the region removed by PARL (Fig. 1A) was reported to inhibit the disaggregase activity of CLPB (Cupo and Shorter, 2020). Therefore, as a validation, we expressed full-length CLPB exogenously in HEK-293T cells, and examined the sizes of protein products. Western blotting analysis showed two clear bands with the precursor form gradually decreasing over time (Supplementary Fig. 1C). Next, another construct harboring the sequence of CLPB starting from PARL cleavage site (named CLPB-N127) was tested for HEK-293T expression, which resulted in a protein product in the same size as the mature form of CLPB (Supplementary Fig. 1D). Therefore, the CLPB-N127 construct was finally used for CLPB protein preparation from *E. coli* cells.

Interestingly, both gel filtration and nsEM showed that the purified CLPB complex is in a higher oligomeric state rather than a hexamer as expected from typical AAA+ unfoldases and disaggregases (Supplementary Fig. 2A and B). And this higher-order organization is irrelevant of exogenously supplemented AMPPNP (Supplementary Fig. 2A). Despite this unusual observation, the purified CLPB complex is competent in both ATPase and disaggregase activities (Supplementary Fig. 1E and F). AMPPNP-treated CLPB complexes were then subjected to cryo-EM analysis. The 2D classification showed a three-layered architecture and a heptameric feature for the side-view and top-view average images, respectively (Fig. 1B). Further 3D classification indicated that CLPB complexes are double-heptamers, and they are extremely dynamic in structure, with both inter- and intra-heptamer conformational variations. With different 3D classification strategies, we could only push the overall resolution to a range of 6-7 Å (Supplementary Fig. 3, S1 Table). At this resolution, secondary structures were resolved in certain regions, and the map matches well with the predicted model of CLPB by AlphaFold (Jumper et al., 2021). The overall size of the complex is 175 Å and 160 Å in height and width, respectively. The seven NBDs form a closed ring, with an open channel (24 Å in diameter) in the center. The “head-to-head” organization of the two heptamers is mediated by their N-terminal ANK domains (Fig. 1C). Although a heptameric form of the ATPase modules is rare among AAA+ ATPases, another mitochondrial AAA+ ATPase Bcs1 was recently reported to exist in a homo-heptamer form (Kater et al., 2020; Tang et al., 2020).

Since the double-heptamer contains no substrate and is widely open in the central pore, we set out to obtain a

structure of the substrate-engaged CLPB complex. A convenient way of doing this is through a Walker B mutation (E425Q) in the NBD domain. For most of the AAA+ proteins, this mutation would greatly slow down ATP hydrolysis but not ATP binding. Structural studies of a few AAA+ unfoldases/disaggregases showed that this mutation often resulted in a co-purification of endogenous peptide in the central channel (Fei et al., 2020; Lo et al., 2019; Twomey et al., 2019). Therefore, we prepared $CLPB^{E425Q}$ mutant from *E. coli* cells (Supplementary Fig. 2C and D) and analyzed the sample by cryo-EM (Supplementary Fig. 4). Unexpectedly, top-view class averages from 2D classification showed a hexameric ring (Fig. 1B and Supplementary Fig. 5B). Similar to the wild type (WT) CLPB complex, the mutant complex is also highly dynamic and the global density map could only be refined to a global resolution of 7.9 Å. With local refinement, the NBD ring was improved to 5.2 Å (Supplementary Fig. 4C, D and F). From the structure, it is clear that the mutant $CLPB^{E425Q}$ now takes a double-hexamer (dodecamer) form. Compared with the WT structure, while the width of the mutant complex reduces from 160 Å to 135 Å, the overall height increases from 175 Å to 200 Å (Fig. 1D). This is due the spiral configuration of $CLPB^{E425Q}$ subunits within each hexamer. From the improved map of the NBD ring, the substrate density in the central channel could be unambiguously identified (Supplementary Fig. 4D). In general, the helical arrangement of subunits within a hexamer is highly similar to other substrate-bound AAA+ ATPases (Cooney et al., 2019; Gates et al., 2017; Twomey et al., 2019).

To confirm that this higher-order organization of CLPB is not an artifact of exogenous expression in *E. coli*, we examined the oligomeric states of CLPB variants purified from HEK-293T cells. The nsEM analysis indicates that both the WT and mutant CLPB complexes derived from human cells display a similar higher-order organization as the *E. coli* ones (Fig. 2A). Next, to rule out the possible splicing isoform specific effect on the oligomeric state, we also examined the isoform-1 of CLPB (UNIPROT: Q9H078-1) purified from *E. coli* cells (Supplementary Fig. 2E-F) using both nsEM and cryo-EM. This isoform-1 is 30 residues longer in the ANK domain than the isoform-2. Our results show that $CLPB^{isoform1}$ complexes are again double-heptamers with an open central channel in the NBD ring (Fig. 2E, Supplementary Fig. 5C).

In short, these results demonstrate mitochondrial CLPB, unlike other typical AAA+ proteins, adopts a unique higher-order structure. The CLPB-specific ANK domain mediates the attachment of two heptamers/hexamers through a head-to-head dimerization. Both the double-heptamer and double-hexamer are highly dynamic. Several

factors contribute to the conformational flexibility of the full-length complexes. The first is the hexamer/heptamer interface. Although the ANK domains from the two heptamer/hexamers interact with each other, they do not have lateral interactions. Thus, the interface between two heptamers/hexamers is rather flexible. The second is the flexibility within each heptamers/hexamers, because the AAA+ domain rings are known to adopt unsymmetrical and dynamic conformations.

Substrate binding induces the transition from double-heptamer to double-hexamer

A major difference between the WT and E425Q CLPB structures is the presence of a peptide substrate in the central pore, which brings close CLPB subunits to form a more compact structure. As shown in the 2D classification results, most of the top-view classes of the WT CLPB particles are heptameric, and only a tiny top-view class, 1.7% of all top-view particles, display a hexameric feature (Fig. 2B-C, Supplementary Fig. 5A). In contrast, all the top-view classes of the $CLPB^{E425Q}$ particles are hexameric exclusively (Fig. 2B-D, Supplementary Fig. 5B). This suggests that the binding of substrate may induce a transition from tetradecamers to dodecamers.

To test this hypothesis, we incubated the WT CLPB complexes with a model substrate casein (Cupo and Shorter, 2020) in the presence of excessive ATPγS, which has been shown to best promote the binding of casein to Hsp104 (Gates et al., 2017; Weaver et al., 2017). As a control, WT CLPB complexes were also treated with ATPγS alone. Cryo-EM 2D classification was employed to analyze their oligomeric states. For the CLPB-ATPγS dataset, only a small fraction (8.0% of all top-view particles) shows a hexameric ring (Fig. 2B and F), indicating that the majority of particles retain the form of double-heptamer. In sharp contrast, in the presence of casein, the percentage of hexameric top-view particles has increased to 51.8% (Fig. 2B and G). These results indicate that substrate binding is likely the most important factor that drives the formation of double-hexamers from double-heptamer.

The ANK domain is essential for the assembly and function of CLPB complexes

To validate the role of the ANK domain in organizing the higher-order structure, we created an NBD-only variant by truncating the N-terminal ANK domain. Gel filtration and nsEM reveal that CLPB-NBD proteins still form oligomers (Supplementary Fig. 9), but the size is much smaller than the double-heptamer or double-hexamer. Thus, these results experimentally proved a role of the ANK domain in assembling the higher-order CLPB complex.

169 Next, we examined whether these CLPB-NBD oligomers have ATPase and disaggregase activities. Our results show
170 that the disaggregase activity critically depends on the integrity of both the ANK and NBD domains. The
171 introduction of E425Q mutation ($CLPB^{E425Q}$ or $CLPB\text{-}NBD^{E425Q}$) and the deletion of ANK domain (CLPB-NBD)
172 both resulted in a complete loss of the disaggregase activity. This is consistent with a previous study (Cupo and
173 Shorter, 2020), suggesting an essential role of the ANK domain in the disaggregase function of CLPB. However, in
174 contrast to the same study, our data show that CLPB-NBD is active in hydrolyzing ATP, and the activity is even
175 higher than the WT CLPB (Supplementary Fig. 6). This discrepancy is due to the fact that CLPB-NBD in that study
176 only formed dimer-like species under their pH 8.0 condition, whereas we used an acidic condition (pH 6.8) that is
177 more relevant to that of the mitochondrial IMS.

178 For functional analysis of the ANK domain, we determined the crystal structure of the ANK domain at 2.1 Å
179 resolution (S2 Table). The ANK domain of CLPB contains four ankyrin motifs (AM) and a unique insertion
180 (consisting of two short helices) between AM2 and AM3 (Fig. 3A, right panel). The isoform 1 of CLPB differs from
181 the isoform 2 exactly in this region, with 30 residues more in this insertion sequence (Fig. 3A, left panel). Since the
182 ANK domain is important for both the assembly and function of CLPB, we wonder whether this insertion is
183 functionally relevant. From the density map of the double-hexamer, the substrate density extends from the RBD
184 ring to the layers of ANK domains, and some extra density in the center of the ANK layers was observed
185 (Supplementary Fig. 7A). Fitting of the crystal structure of the ANK domain reveals that the insertion exactly locates
186 in the inner surface of the ANK layers. Interestingly, the insertion contains two patches of hydrophobic residues
187 (Fig. 3B), implying a potential role in substrate binding. Therefore, we constructed another CLPB mutant with the
188 insertion completely deleted ($CLPB^{\Delta 201\text{-}232}$), and compared this mutant with both isoforms 1 and 2 in their ATPase
189 and disaggregase activities. The $CLPB^{\Delta 201\text{-}232}$ mutant showed the same oligomeric state as the isoforms 1 and 2
190 (Supplementary Fig. 7C to E). The two isoforms have comparable activities in these two molecular functions (Fig.
191 3C). Although the deletion in $CLPB^{\Delta 201\text{-}232}$ had no effect on the ATPase activity, it reduced disaggregase activity
192 sharply by more than 50% (Fig. 3C and D). Therefore, this insertion is likely involved in the substrate recognition
193 and may also contribute to the translocation of the substrate to the C-terminal NBD ring.

194 Next, we analyzed the dimer interface of the ANK domain by docking the ANK models into the density maps
195 of the double-heptamer and double-hexamer (Supplementary Fig. 8A and B). The ANK dimers in the two higher-

order structures are not identical but generally similar. For the ANK dimer in the double-hexamer, two regions of the ANK domain contribute to the dimerization, the AM1/2 motifs and the insertion (Fig. 3G). One interface is relatively extensive and formed by four connecting loops between the first and second helices of the AM1 or AM2 from the two opposite ANK domains. The other interface is mediated by the second helix (and its downstream flanking sequence) of the insertion, and two arginine residues, R178 and R227, appear to be important in this interface. Based on the electrostatic surface potential, these two residues of one ANK domain point to a highly negatively charged surface patch (E140, E221, D222 and D223) of the opposite ANK domain (Fig. 3G). In fact, both R178 and R227 are highly conserved among the metazoan species (Cupo and Shorter, 2020). Therefore, we performed mutagenesis (R178E and R227E) to test whether they could disrupt the ANK dimerization. Unexpectedly, the two CLPB mutants still maintain a higher-order assembly, but their disaggregase activities are severely impaired by 70-80% (Fig. 3E and F, and Supplementary Fig. 8C-E). These results further emphasize a role of the ANK domain in the disaggregase function of CLPB.

Altogether, we demonstrate that the ANK domain is essential for both the assembly and function of the CLPB complex, and the functional importance of the ANK domain could be largely attributed to its insertion sequence between the AM2 and AM3.

CLPB-NBD assembles into polypeptide-engaged helical structures

Due to the large inter- and intra-hexamer/heptamer flexibility, the structures of full-length CLPB complexes were not solved in atomic resolution. CLPB-NBD was thus used as a surrogate for high-resolution structural determination. Two mutant versions of CLPB (NBD and NBD^{E425Q}) were analyzed by cryo-EM (Supplementary Fig. 9A-F), which again confirmed that E425Q mutation resulted in co-purification of an endogenous peptide in the central channel. Also similar to the full-length complexes, the top-view classes of the NBD^{E425Q} particles are exclusively hexameric, whereas both hexameric and heptameric arrangements were observed for the NBD^{WT} particles (Supplementary Fig. 9F). Subsequently, we focused on the NBD^{E425Q} dataset for high-resolution refinement. After several rounds of 3D classification, three different oligomeric arrangements, hexameric, heptameric and nonameric, were identified. The nonamer appeared to be more stable and could be resolved at an overall resolution of 3.7 Å (Supplementary Fig. 10), allowing the atomic modelling of the NBD of CLPB. In the nucleotide-binding

223 pockets of the nonamer, a total of eight ATP molecules could be modelled (Supplementary Fig. 11). The conserved
224 functional motifs on the ATPase domain are well resolved, including the Walker A motif (351-GSSGIGKT-358),
225 sensor-1 (464-TSN-466), and sensor-2 (588-GAR-590) (Fig. 5E). The conserved residues I317, I318 and F541 form
226 a hydrophobic pocket to stabilize the adenine ring of ATP, while T358 stabilizes the β- and γ-phosphates through a
227 Mg^{2+} ion (Fig. 5E). The Arginine Finger (R531) from the adjacent protomer points to the γ-phosphate of ATP. In
228 general, these structures show that the NBD of CLPB is a typical AAA+ ATPase module, underscoring a conserved
229 mechanism of ATP-powered substrate unfolding and translocation (Gates and Martin, 2020).

230 The central channels of all three states are occupied by a peptide substrate, which forms successive interactions
231 with the helically arranged CLPB protomers (Fig. 4A-C). In the nonamer, 9 protomers form a 1.5-turn helix around
232 the central substrate. Besides the protomer number, the three oligomers also show obvious structural differences.
233 While the twist angle between neighboring subunits is roughly 60° in all three forms, the axial rise within each
234 oligomer is not constant and varies in the hexamer and heptamer largely. The axial displacements between P1 and
235 P6 are roughly 25 Å, 30 Å and 35 Å for the hexamer, heptamer and nonamer, respectively (Fig. 4D-F). This is
236 expected, as more axial space is required to fit in the seventh and more subunits onto the hexamer. In the full-length
237 complexes, the ANK domain provides a steric hindrance to end the helical extension.

238 Overall, these data show that the ANK domain is essential in determining the oligomeric state of CLPB
239 complex, and also explain why our CLPB-NBD still retains ATPase activity. Although this nonameric helical
240 structure does not exist in a physiological context, it demonstrates that CLPB-NBD shares many characteristics of
241 typical AAA+ proteins.

242

243 **The substrate interacts with conserved pore-loops of the helically arranged NBDs**

244 The density of the polypeptide backbone is well resolved in the nonamer and was modeled as a 17-residue
245 poly-alanine fragment (Fig. 5A and B). The peptide spans about 53 Å length in the central channel of the nonamer
246 and displays successive interactions with the PL-I and PL-II from NBD protomers (Fig. 5B). For each protomer, a
247 canonical PL-I (399-GYVG-402) binds to the peptide through two hydrogen bonds formed between the main-chain
248 atoms. The first is between the carbonyl oxygen of the substrate residue N and the main-chain nitrogen of V401,
249 and the other between the carbonyl oxygen of G399 and the main-chain nitrogen of the substrate residue N+2 (Fig.

250 5C). This pattern of interactions is nearly identical for all protomers, except that the hydrogen bond distances vary
251 between 2.5-4.0 Å. Thus, the axial step size of PLs is exactly two residues. Of note, the main-chain atoms of Y400
252 do not participate in sequence-independent interaction with the substrate backbone. Therefore, the essential role of
253 Y400 in the disaggregase activity should arise from its aromatic side-chain, which could interact with various side-
254 chains of a threaded substrate. Moreover, the substrate could be modeled in both directions (N to C or C to N) in
255 the density map, and both configurations could satisfy this repeated pattern of interactions (Fig. 5C and D). In
256 contrast to the PL-I, the PL-II, consisting of E386, R387, and H388, is relatively away from the substrate backbone,
257 except that the side-chain of H388 is within 4-Å distance with the β-carbon atom of the substrate (Fig. 5B). Thus,
258 it is likely that the primary role of PL-II during substrate processing is to interact with different side-chains of the
259 substrate through its polar residues.

260 In short, these results indicate that the NBD ring of CLPB is a typical unfoldase core, and the PLs of CLPB
261 functions to grip and move the substrate within the central channel in a conserved manner as classic AAA+
262 unfoldases/disaggregases.

263

264 **Mitochondrial interactome analysis of the ANK domain**

265 Previous data showed that *CLPB* knockout cells exhibited decreased solubility for many proteins in the IM
266 and IMS of mitochondria, including HAX1, TOMM22/70, TIMM22/23, HTRA2, PHB1/2, OPA1, STOML2 and
267 SLC25 family proteins (Cupo and Shorter, 2020). Given the essentiality of the ANK domain in the disaggregase
268 activity of CLPB, we performed a mass spectrometry (MS) based interactome analysis of the ANK domain. A
269 plasmid harboring the MTS and ANK domain sequences was expressed in HEK-293T cells, and mitochondria were
270 then isolated, lysed and dissolved in 1% detergent. The ANK domain and its binders were purified through a C-
271 terminal Strep tag, and subject to MS analysis. A relatively stringent criterion (fold-change > 4 and p-value < 0.01)
272 were used for enrichment analysis (three biological replicates). With DAVID Bioinformatics Resources (Sherman
273 et al., 2022), we restricted our analysis on mitochondrial proteins detected in the samples. Compared with the control
274 sample, 934 mitochondrial proteins were significantly enriched in the ANK sample, and most of them are located
275 in the IM and matrix (60.3%). Although CLPB is located in the IMS, it may also function to promote the solubility
276 of certain membrane proteins with IMS-exposed domains. Therefore, we focused on proteins from the OM, IMS

277 and IM. As a result, 381 such proteins were selected for further analysis, including all of those potential substrates
278 previously reported to be most affected by *CLPB*-knockout (Cupo and Shorter, 2020). If these proteins were ranked
279 by their abundances, three IMS proteins stood out in the top-20 list, including HAX1, OPA1 and AGK (Fig. 6C).
280 Consistently, both HAX1 and OPA1 have been experimentally validated to interact with CLPB (Chen et al., 2019b;
281 Fan et al., 2022). In general, the ANK interactome identified in this study agrees well with previous proteomic data
282 based on full-length CLPB (Chen et al., 2019b; Fan et al., 2022; Wakula et al., 2020), indicating that the ANK
283 domain has a direct role in substrate binding.

284 We also showed that the unique insertion between AM2 and AM3 in the ANK domain is important in the
285 disaggregase activity *in vitro* (Fig. 3). Therefore, two ANK variants were next used for interactome analysis. The
286 MTS-ANK$^{\Delta 201\text{-}232}$ and MTS-ANK$^{\text{isoform1}}$ were expressed in HEK-293T cells and their interactome were similarly
287 analyzed by MS (Fig. 6D). Among the analyzed mitochondrial OM, IMS and IM proteins, eight proteins were more
288 enriched in the ANK$^{\text{isoform2}}$ sample, including ATAD3B/ATAD3A, SLC25A4/5/12/13, HAX1 and DNM1L. All of
289 them are indeed among the most abundant top-20 list. In contrast, a larger number of proteins (fourteen) were
290 selectively enriched in the ANK$^{\text{isoform2}}$ sample than the ANK$^{\Delta 201\text{-}232}$ sample, again including HAX1 and DNM1L
291 (Fig. 6E, S6 Table). Very interestingly, a recent study reported that HAX1 preferentially binds to the isoform 2 of
292 CLPB *in vivo*, rather than the isoform 1 (Fan et al., 2022), highly consistent with our findings.

293 These interactome analyses support a direct role of the ANK domain in substrate binding, and together with
294 previous studies (Chen et al., 2019b; Cupo and Shorter, 2020; Fan et al., 2022) confirmed that HAX1 is one of the
295 natural substrates of CLPB. The differential enrichment between the isoform1 and 2 further suggests a possible role
296 of the ANK insertion in substrate selection, probably through altered binding affinity.

297

298 **Discussion**

299 In the present work, we characterized the structures of CLPB in both the apo and substrate-bound states.
300 Unexpectedly, we found that apo CLPB assembles into higher-order structures, in the form of a double-heptamer
301 through inter-molecular interactions mediated by N-terminal ANK domains (Fig. 1). We further demonstrate that
302 the double-heptamers could be efficiently converted to double-hexamers upon the addition of a model substrate
303 (Fig. 2), highlighting the possibility that the double-heptamer is a physiologically relevant, resting state of CLPB
304 in mitochondria. We believe that the heptameric form of CLPB is not a pure *in vitro* artifact for several reasons.

305 First, the heptamer form is the predominant species of apo CLPB (Fig. 2), indicating an intrinsic property of the
306 CLPB ATPase module. Although AAA+ proteins are generally considered to be hexamers, an increasing number of
307 AAA+ proteins were recently discovered to take heptamer as a primary oligomeric state (Hoffmann et al., 2022;
308 Kater et al., 2020; Kim et al., 2020; Tang et al., 2020), including a mitochondrial IM-bound AAA+ protein Bcs1
309 (Kater et al., 2020; Tang et al., 2020). Second, The substrate-induced change on the oligomeric state has also been
310 observed for other AAA+ members, such as DNA helicase AAV2 Rep68 (Santosh et al., 2020), RuvB (Miyata et
311 al., 2000), and archaeal MCM (Yu et al., 2002). Third, the ATPase activity of full-length CLPB (double-hexamer)
312 is lower than CLPB-NBD alone (Supplementary Fig. 6). In fact, roughly two third of CLPB-NBD particles exhibit
313 a hexameric arrangement. This indicates that the heptamer is not optimized for efficient ATP-hydrolysis. Thus, as a
314 substrate-free state, the heptameric form could avoid necessary ATP consumption in the IMS. Notably, the buffer
315 we used to prepare CLPB complexes was at pH 6.8, which closely resembles that of the IMS (Santo-Domingo and
316 Demaurex, 2012).

317 Nevertheless, with these said, the substrate-engaged CLPB is still hexameric as shown in the structures of
318 $CLPB^{E425Q}$ and NBD. In the high-resolution structure of the NBD^{E425Q} nonamer, the PL-Is of the nine protomers
319 form a spiral staircase around the substrate in a two-residue step-size (Fig. 5C-D). There PL-Is interact with the
320 substrate in a sequence-independent manner, and capable of accommodating polypeptide in both the N-C and C-N
321 directions, implying that it could potentially thread the substrate in both directions, similar as bacterial ClpX and
322 ClpA (Olivares et al., 2017). These data indicate that the mechanisms of CLPB in substrate threading and
323 translocation are highly similar to those cytosolic AAA+ unfoldases/disaggregase, such as Cdc48/p97 and Hsp104
324 (Cooney et al., 2019; Gates et al., 2017; Pan et al., 2021; Twomey et al., 2019).

325 In the double-hexamer, both hexamers are in active conformation with the substrate being threaded through
326 the central pores of their ATPase rings. This raises an interesting question: Whether or not the two hexamers work
327 in a synergistic manner, since a CLPB hexamer already contains all essential structural features of a
328 unfoldase/disaggregase. A conventional model is that the two hexamers work independently, and upon engagement
329 with a protein aggregate the two hexamers do not need to maintain stable association for all six pairs of ANK
330 domains. However, as seen in the structure of the double-hexamer (Fig. 1D), it is also possible that the axial
331 movement of a CLPB subunit in one hexamer during the ATP-hydrolysis cycle could potentially affect another

332 CLPB subunit in the other hexamer through their tightly associated ANK domains. Unfortunately, our attempt to
333 obtain ANK mutants to separate its roles in structural organization and disaggregase activity has failed (Fig. 3E and
334 F). Nevertheless, this "head to head" organization reminds us of the recent findings on the double-hexamer form of
335 p97 (Caffrey et al., 2021; Gao et al., 2022; Hoq et al., 2021; Yu et al., 2021), although p97 utilizes a "back to back"
336 interface through two C-terminal ATPase rings. These two examples underline a possibility that AAA+ proteins
337 could adopt different higher-order assemblies to serve different purposes.

338 We also determined the crystal structure of the ANK domain, and analyzed its functional significance in the
339 disaggregase function. Our data showed that the ANK domain is indispensable for the disaggregase activity of
340 CLPB, and a deletion of the unique insertion in the ANK domain resulted in more than 50% reduction on the
341 disaggregase activity (Fig. 3D). Furthermore, two single mutations of the ANK domain in the ANK dimer interface,
342 including 178E and R227E, both greatly impaired the disaggregase activity by 70-80% (Fig. 3F). R227 is exactly
343 located to the insertion sequence. These observations suggest that this unique insertion is functionally important.
344 Since this insertion is at the innermost position of the ANK ring and distant from the pore-loops of the ATPase
345 modules, the ANK domain may function to recognize and pass the substrate to the distal ATPase ring. This
346 hypothesis was further supported by our interactome analysis of the separate ANK domain. A large number of the
347 IM and IMS proteins were greatly enriched in the sample affinity-purified through tagged ANK, including all of
348 those previously found to be prone to aggregation in Δ*CLPB* cells (Cupo and Shorter, 2020). Many of these
349 candidates have also been reported to interact with CLPB in previous large-scale proteomics studies (Botham et al.,
350 2019; Huttlin et al., 2021), and two of them have been experimentally validated, such as HAX1 and OPA1 (Chen
351 et al., 2019b; Fan et al., 2022). Of note, several mitochondrial proteins involved in cristae remodeling are among
352 the most enriched group, including OPA1, DNM1L, and IMMT. This appears to collaborate with the previous
353 finding that CLPB loss resulted in altered cristae structure in mitochondria (Chen et al., 2019b). We also tested the
354 $ANK^{\Delta 201\text{-}232}$ and $ANK^{isoform1}$ in interactome analysis. Compared with the $ANK^{isoform2}$, a relative extensive change on
355 the enrichment profile was observed for the $ANK^{\Delta 201\text{-}232}$ sample. In contrast, comparison between isoform 1 and
356 isoform 2 reveals that many potential substrates of CLPB are significantly more enriched in the sample of
357 $ANK^{isoform2}$, including HAX1 and DNM1L (Fig. 6E and F). These results further pinpoint a role of the ANK-
358 insertion in the substrate recruitment, and suggest another level of regulation on CLPB function through alternative

splicing.

The structures of CLPB also allow us to map disease related mutations (Capo-Chichi et al., 2015; Cupo and Shorter, 2020; Kanabus et al., 2015; Kiykim et al., 2016; Pronicka et al., 2017; Saunders et al., 2015; Wortmann et al., 2021; Wortmann et al., 2015) on the atomic model to understand their possible effect on the function of CLPB. Mutations associated with 3-MGA could be categorized into three classes. The first class of mutations lie at the interface between two adjacent CLPB protomers, including R378G, R445Q, Y587C, R598C and E609K (Fig. 7A). These mutations likely perturb the inter-protomer communication to impair CLPB function. The second class consists of M381I, C456R, E471K, and Y537C in the large subdomain, and A561V, G616V, R620P, and I652N in the small subdomain (Fig. 7B). These mutations are away from the inter-protomer or inter-domain interfaces, and they may destabilize the domain structure of CLPB (Fig. 7B). The third class of mutations are in the AM3 of the the ANK domain. Besides two nonsense mutations (R250* and K321*), three mutations (T238M, A239T and Y242C) are on the first helix of the AM3 (Fig. 7C). This region contains a characteristic tetrapeptide (-TPLH-) motif (238-TALH-241 in CLPB), and is highly conserved among ankyrin motifs (Li et al., 2006). Therefore, these mutations might destabilize the structure of the ANK domain, or lead to misfolding of the ankyrin motifs. Consistently, it was shown that T238M did not affect the ATPase activity, but largely inhibited the disaggregase activity (Cupo and Shorter, 2020). As for mutations related to SCN, they are exclusively located close to the active center of the NBD (Fig. 7D). They are distributed in sensor-1 (N466K), sensor-2 (R590C), AF (R531Q/G), and Walker A motif (T358K). It is apparent that they may affect the binding and hydrolysis of ATP (Fig. 5E). Indeed, CLPB with these mutations were defective in both the ATPase and disaggregase activities *in vitro* (Warren et al., 2022).

Methods

Protein expression and purification

The coding sequence (isoform 2) of human *CLPB*, amplified from a home-made cDNA library of HEK-293T cells, was cloned into pET28a vector with a N-terminal His6-SUMO tag followed by a TEV protease cleavage sequence, and expressed in *E. coli* Transetta (DE3) cells (Trans). CLPB protein variants were purified as reported previously (Mroz et al., 2020), with some modifications. Briefly, the culture was induced with 1mM IPTG at OD_{600}

386 of 0.6-0.8 at 20°C overnight. Cells were harvested and resuspended in lysis buffer (50 mM Tris-HCl, pH 8.0, 500
387 mM NaCl, 5% glycerol, 1% Triton X-100 and 1mM PMSF) and lysed by sonication. Lysates were cleared by
388 centrifugation in a JA-25.50 rotor (Beckman) for 30 min at 20,000 r.p.m. and the supernatants were precipitated
389 with ammonium sulfate at 35% saturation, then incubated for 10 min at room temperature (RT). The cloudy lysates
390 were centrifuged for 30 min at 15,000 r.p.m., and then dissolved the protein pellet with Buffer B (50 mM Tris-HCl,
391 pH 8.5) supplemented with 5 mM DTT and centrifugation again. The solutions were loaded onto a Mono Q column
392 (GE Healthcare). Proteins were eluted with a linear gradient to 60% Buffer C (50 mM Tris-HCl, pH 8.5, 1M NaCl).
393 To remove His6-SUMO tags, TEV protease was added into the eluates, and then incubated at RT for 2 hrs. The tag
394 and contaminations were removed by size-exclusion chromatography, which was pre-equilibrated with 20 mM
395 HEPES-KOH, pH 6.8, 300 mM KCl, 5 mM $MgCl_2$. Peak fractions were pooled and concentrated, then incubated
396 with 5 mM nucleotide (AMPPNP for CLPB, ATP for $CLPB^{E425Q}$) at RT for 2 hrs. 1 mM BS3 was added to improve
397 the sample stability, and loaded onto size-exclusion chromatography. Peak fractions were first examined by nsEM,
398 then pooled and concentrated. 1mM nucleotide was added before vitrification. $CLPB^{E425Q}$ and $CLPB^{Y400A}$ were
399 prepared by site-specific mutagenesis, and purified as described above.

400 The NBD and NBD^{E425Q} sequences were cloned by site-specific mutagenesis. Harvested cells were resuspended
401 in lysis buffer II (50 mM Tris-HCl, pH 7.4, 300 mM NaCl, 5% glycerol, 1% Triton X-100, 1 mM PMSF, and 20
402 mM imidazole) and lysed by sonication. The supernatants were incubated with Ni–NTA agarose beads (GE
403 Healthcare) at 4°C for 2 hrs. After washed 5 times with lysis buffer, protein was eluted with elution buffer (50 mM
404 Tris-HCl, pH 7.4, 300 mM NaCl, 5 mM $MgCl_2$, and 500 mM imidazole). TEV protease was add into the eluates to
405 remove His6-SUMO tags, and then incubated at RT for 2 hrs. Then the proteins were loaded onto size-exclusion
406 chromatography, which was pre-equilibrated with 20 mM HEPES-KOH, pH 6.8, 300 mM KCl, 5 mM $MgCl_2$. Peak
407 fractions were pooled and concentrated, then incubated with 5 mM nucleotide (AMPPNP for NBD, ATP for
408 NBD^{E425Q}) at RT for 2 hrs, and then loaded onto size-exclusion chromatography. Peak fractions were first examined
409 by nsEM, then pooled and concentrated. 1mM nucleotide was added before vitrification.

410 For the ANK domain purification, cells were resuspended in lysis buffer III (50 mM Tris-HCl, pH 8.0, 500
411 mM NaCl, 5% glycerol, 1% Triton X-100, 1 mM PMSF, and 20 mM imidazole). The supernatants were incubated
412 with Ni–NTA agarose beads (GE Healthcare) at 4°C for 2 hrs. The eluates were loaded onto size-exclusion

413 chromatography, and eluted with 50 mM Tris-HCl, pH 8.0, 150 mM NaCl.

414

415 **ATPase activity measurement**

416 0.1 μM CLPB and CLPB variants were incubated with 1 mM ATP at 30°C for 30 min in ATPase activity buffer
417 (AAB: 20 mM HEPES-KOH, pH 6.8, 150 mM KAOc, 5 mM $MgCl_2$, 0.1% Tween-20). ATPase activity was
418 measured by using the Malachite green phosphate assay (Lanzetta et al., 1979). For each protein at least two
419 biological replicates were measured with three independent replicates.

420

421 **Luciferase disaggregation assay**

422 Disaggregase activity was measured as previously reported (Cupo and Shorter, 2020). Briefly, 1 μM CLPB and
423 CLPB variants were incubated with 50 nM fresh firefly luciferase aggregates at 30°C for 90 min in luciferase
424 reactivation buffer (LRB: 20 mM HEPES-KOH, pH 8.0, 150 mM KAOc, 10 mM KAOc, 10 mM DTT)
425 supplemented with 5 mM ATP. Notably, the disaggregase activity of CLPB was detected using the luciferase
426 reporter assay kit (Beyotime, CAT# RG005) alone (Supplementary Fig. 1F). Others were detected with the
427 luciferase reporter assay kit (Trans, CAT# FR101-01).

428

429 **Transient overexpression of CLPB variants**

430 HEK-293 T/F cells were transfected with pCAG vector containing CLPB variants. Cells were transfected using pEI
431 transfection reagent. After 48 hrs, cells were collected.

432

433 **Western blots**

434 Cells were washed with PBS and incubated with lysis buffer B (50 mM Tris-HCl pH 7.4, 150 mM NaCl, 1%
435 Triton X-100, 0.1 % SDS and 1mM PMSF) for 30 min on ice. α-Strep antibody (Huaxing Bio, CAT# HX1816) was
436 used to detect the target protein.

437

438 **Mitochondrial isolation**

439 Mitochondria were isolated as previously described (Cupo and Shorter, 2020; Frezza et al., 2007). Briefly, 800

440 mL cells were resuspended in 40 mL mitochondria isolation buffer (20 mM HEPES-KOH, pH 7.6, 250 mM sucrose
441 and 2 mM EDTA) and homogenized with a Dounce homogenizer at 4°C. Lysate was then centrifuged at 1,300g for
442 5 min. The supernatant was collected and then centrifuged at 13,000g for 15 min twice. And the pellet was
443 resuspended with lysis buffer C (20 mM Tris-HCl pH 8.0, 150 mM NaCl, 1% Triton X-100, and 1mM PMSF) and
444 incubated for 30 min at 4°C. Lysate was then centrifuged at 20,000g for 30 min. The supernatant was collected and
445 incubated with Strep resin for 2 hrs at 4°C. After extensively washed, SDS-loading buffer was added to the sample.
446 The samples were separated by MOPS-PAGE on a gradient gel (4%-20%).
447
448 **LC-MS/MS analysis**
449 The samples were excised into several parts form protein gels, reduced with DTT, alkylated with iodoacetamide
450 (IAA), and subsequently digested with trypsin. Peptides were analyzed by Thermo Orbitrap Exploris 480 mass
451 spectrometer (Thermo Fisher Scientific) coupled with an Easy LC system (Thermo Fisher Scientific). Peptides
452 mixtures were loaded onto C18 Trap Column in Buffer A (0.1% formic acid) and separated with a gradient Buffer
453 B (0.1% formic acid, 80% ACN) (2 min 4-8% B; 37 min 8-25% B; 11 min 25-35% B;7 min 35-95% B; 3min 95%
454 B) at a flowrate of 300 nL/min. Data were acquired in data-dependent mode with s with the following settings: MS1
455 60,000 resolution, 300 to 1650 m/z of mass range; MS2 30% normalized collision energy, 15,000 resolution, 1.6
456 m/z of isolation window. Proteins were identified and quantified by Proteome Discoverer software 2.2 using default
457 settings against a database of UNIPROT *Homo sapiens*. Methionine oxidation and N-terminal acetylation were set
458 as variable modifications. Protein level and peptide level false discovery rate (FDR) was set at 1%.
459 The differential enrichment analyses were based on three biological replicates (starting from expression plasmid
460 transfection), and a stringent screening condition (p-value < 0.01 and Fold change > 4) was used. In the MTS-ANK-
461 Strep samples, 1,115 mitochondrial proteins were detected, of which 934 proteins were highly enriched, compared
462 with the MTS-HA sample (S3 Table). From these highly enriched proteins, those located in the OM, IMS and IM
463 were selected for further analysis (S5 Table, Fig 6C). The comparison between the MTS-ANK-Strep and MTS-
464 $ANK^{\Delta 201-232}$-Strep samples was focused on 374 mitochondria proteins with OM, IMS and IM locations (S6 Table).
465 The comparison between the MTS-ANK-Strep and MTS-$ANK^{isoform1}$-Strep samples was similarly done, and 332
466 OM, IMS and IM proteins were used for analysis.

467

468 **Cryo-EM specimen preparation**

469 The sample homogeneity was first examined by nsEM. Proteins were applied onto carbon-coated copper grids,
470 and examined with an FEI Tecnai T20 TEM at 120 kV. During specimen preparation for cryo-EM, CLPB and
471 $CLPB^{E425Q}$ particles displayed strong preferred orientation. 0.5 mM CHAPSO was added to reduce the preferred
472 orientation (Chen et al., 2019a). Cryo-grids (R1.2/1.3, Au300, Quantifoil) were prepared with an FEI Vitrobot
473 Mark IV with the chamber set at 6°C and 100% humidity. Grids were screened with an FEI Talos Arctica before
474 data collection.

475

476 **Cryo-EM data collection and image processing for CLPB**

477 For the sample of CLPB-AMPPNP, micrographs were recorded with 300 kV FEI Titan Krios (Gatan K3 direct
478 electron detector) with GIF Quantum energy filter (Gatan) at a nominal magnification of 81,000X and at a
479 calibrated pixel size of 1.07 Å. 40 frames with exposure time of 3.2 s were collected with defocus ranged from
480 -1 to -1.4 μm under low-dose condition. A total of 9,341 micrographs from two datasets were collected with
481 EPU. The micrographs were subjected to beam-induced motion correction using MotionCor2 (Zheng et al.,
482 2017), and contrast transfer function (CTF) parameters for each micrograph were determined by Gctf (Zhang,
483 2016). RELION (versions 3.1) was used to perform data processing (Zivanov et al., 2020). After auto-picking,
484 the particles were subjected to 2D classification and several round 3D classifications. 299,306 particles from
485 two datasets were selected and applied for the next round of 3D classification (K=4), a final set of 231,212
486 particles were kept for 3D refinement. For double-heptamer, another round of 3D classification (K=6) without
487 alignment was performed to improve the resolution. Finally, 153,005 particles were kept for the final 3D
488 refinement (final resolution 6.8 Å). Due to the inter-heptamer flexibility, mask-based (only including a single
489 heptamer) classification (K=6) and refinement was applied, which showed no significant improvement
490 (Supplementary Fig. 3). In addition, multiple rounds of focused classification based on the NBD-ring or a
491 selected combination of CLPB subunits using symmetry expansion derived half-particles were also tried, with
492 different setting of parameters, however, none of them was able to reach better than 5 Å resolution.

493 For the sample of $CLPB^{E425Q}$-ATP, micrographs were recorded with 300 kV FEI Titan Krios (Gatan K2 camera)

with GIF Quantum energy filter (Gatan) at a nominal magnification of 36,000X and at calibrated pixel sizes of 1.052 Å. 32 frames with exposure time of 8 s were collected with defocus ranged from -1.2 to -1.8 μm under low-dose condition. A total of 4,574 micrographs were collected with SerialEM (Mastronarde, 2005). After 2D classification and several round 3D classifications, a 7.5-Å density map was achieved (Supplementary Fig. 4). In Addition, a density map of 5.2-Å could be achieved by applying a local mask of the NBD-ring during reconstruction (Supplementary Fig. 4C, D and F).

For the sample of $CLPB^{isoform1}$-AMPPNP, a total of 953 micrographs were recorded with 200 kV FEI Titan Krios (Gatan K2 camera) at a magnification of 36,000X and at calibrated pixel sizes of 1.157 Å. 32 frames with exposure time of 8 s were collected with defocus ranged from -1.1 to -1.8 μm under low-dose condition. After several rounds of 2D classifications, only hexameric rings of top views were observed (Supplementary Fig. 5C).

For the sample of CLPB-casein-ATPγs, 20 μL casein (4.0 mg/mL) was added into 40 μL CLPB (2.0 mg/mL) before vitrification. A total of 885 micrographs were recorded with 200 kV FEI Titan Krios (Gatan K2 camera) at a magnification of 36,000X and at calibrated pixel sizes of 1.157 Å. 32 frames with exposure time of 8 s were collected with defocus ranged from -1.4 to -2.0 μm under low-dose condition. After several rounds of 2D classifications, 54,771 particles were left, and hexameric rings (25,867 particles) and heptameric rings (24,046 particles) of top views were both observed (Supplementary Fig. 5D). As a control, CLPB-ATPγs dataset was prepared as CLPB-casein-ATPγs without adding casein.

For the sample of NBD^{E425Q}-ATP, micrographs were recorded with 300 kV FEI Titan Krios G3i (Gatan K3 direct electron detector) with GIF Quantum energy filter (Gatan) at a magnification of 64,000X and at pixel size of 1.08 Å. 32 frames with exposure time of 2.44 s were collected with defocus ranged from -1 to -1.4 μm. A total of 4,574 micrographs were collected. 3,753,541 particles were split into 2 parts to facilitate processing. After several rounds of 2D classification and 3D classification, 3 major classes were found: hexamer, heptamer, and nonamer. A small group of hexamer particles were used for 3D refinement, resulting in a density map of 7.4 Å (Supplementary Fig. 10). The particles of heptamer and nonamer were subjected additional rounds of 3D classification, and after CTF refinement and Bayesian polishing, were reconstructed to the final resolutions of 4.1 Å and 3.7 Å, respectively (Supplementary Fig. 10).

For the sample of NBD^{WT}-AMPPNP, a total of 720 micrographs were recorded with 200 kV FEI Titan Krios

521 (Gatan K2 camera) at a magnification of 36,000X and at calibrated pixel sizes of 1.157 Å. 32 frames with
522 exposure time of 8 s were collected with defocus ranged from -1.2 to -2.0 μm under low-dose condition. After
523 2D classification, both hexameric rings and heptameric rings of top views were observed (Supplementary Fig.
524 9).
525 Data collection and processing were summarized in S1 Table.
526
527 **Crystallization, data collection, and structure determination of the ANK domain**
528 Plate-shaped crystals of CLPB-ANK were obtained within 3 weeks by sitting drop vapor diffusion method at
529 16°C. Typically, a volume of 1 μL of protein solution at a concentration of 6-12 mg/mL in the GF buffer (5 mM
530 Tris-HCl, pH 7.5, 100 mM NaCl) was mixed with an equal volume of a precipitant well solution of 0.2 M
531 Ammonium citrate tribasic, pH 7.0, 20% (w/v) Polyethylene glycol 3,350. Crystals were directly frozen and stored
532 in liquid nitrogen prior to data collection. The final data set was collected at the Shanghai Synchrotron Radiation
533 Facility (SSRF) beamline BL18U1 (wavelength = 0.97915 Å, temperature = 100K). A 900 diffraction images were
534 collected with oscillation step of 0.2°. The data were merged and scaled using XDS (Kabsch, 2010) and Aimless
535 (Evans, 2011). The initial structure solution was obtained using the molecular replacement program PHASER
536 (McCoy et al., 2007) followed by AutoBuild (Terwilliger et al., 2008) with a prediction structure of CLPB by alpha-
537 fold (Jumper et al., 2021). Further model building was done using Coot and Phenix (Adams et al., 2010; Emsley
538 and Cowtan, 2004), respectively. Data collection and refinement statistics are summarized in (S2 Table) and the
539 atomic coordinates and structure factors have been deposited in the protein data bank (PDB ID: 7XC5).
540
541 **Model building and refinement**
542 Model building was based on the prediction structure of CLPB by AlphaFold (Jumper et al., 2021) and the crystal
543 structure of the ANK domain. The models were first docked into the cryo-EM density map using UCSF Chimera
544 (Pettersen et al., 2004), rebuilt manually in Coot and refined (real-space) using Phenix (Adams et al., 2010; Emsley
545 and Cowtan, 2004). Figures preparation and structure analysis were performed with and UCSF ChimeraX (Pettersen
546 et al., 2021) and Chimera (Pettersen et al., 2004).
547

548 **Data availability**

549 The cryo-EM density maps have been deposited in the Electron Microscopy Data Bank with the accession codes
550 EMDB-33105, EMDB-33106, EMDB-33109, EMDB-33110 and EMDB-33104 for the CLPB, CLPB^{E425Q},
551 NBD^{E425Q}-hexamer, NBD^{E425Q}-heptamer and NBD^{E425Q}-nanomer, respectively. The atomic model of NBD^{E425Q}-
552 nanomer has been deposited in Protein Data Bank with accession code PDB 7XBK.

553 The coordinate and the structure factor of CLPB-ANK have been deposited in the Protein Data Bank with
554 accession code 7XC5.

555

556 **Acknowledgments**

557 We thank the Core Facilities at the School of Life Sciences, Peking University for help with negative staining
558 EM; the Electron Microscopy Laboratory and Cryo-EM Platform for help with data collection; the High-
559 performance Computing Platform for help with computation; the National Centre for Protein Sciences at Peking
560 University for assistance with mass spectrum. The work was supported by the National Science Foundation of China
561 (31725007 to N.G., 31922036 to N.L.), the National Key Research and Development Program of China
562 (2019YFA0508904 to N.G.), and the Qidong-SLS Innovation Fund to N.G.

563

564 **Author contributions**

565 D.W. prepared the protein samples (with the help of Y.D.), collected the cryo-EM data, performed EM analysis
566 (with the help of G.W., Y.C., and N.G.), and carried out functional experiments. N.G. and D.W. performed model
567 building and wrote the manuscript. D.W., Y.L., G.L. and J.L. purified the ANK domain and performed the
568 crystallization, data collection, and structure determination.

569

570 **Competing interests**

571 Authors declare no competing interests.

572

573 **Correspondence and requests for materials** should be addressed to N.G. and J.L.

574

575 **Reference**

576 Adams, P.D., Afonine, P.V., Bunkoczi, G., Chen, V.B., Davis, I.W., Echols, N., Headd, J.J., Hung, L.W., Kapral, G.J., Grosse-

Kunstleve, R.W., *et al.* (2010). PHENIX: a comprehensive Python-based system for macromolecular structure solution. Acta Crystallogr D Biol Crystallogr *66*, 213-221.

Botham, A., Coyaud, E., Nirmalanandhan, V.S., Gronda, M., Hurren, R., Maclean, N., St-Germain, J., Mirali, S., Laurent, E., Raught, B., *et al.* (2019). Global Interactome Mapping of Mitochondrial Intermembrane Space Proteases Identifies a Novel Function for HTRA2. Proteomics *19*, e1900139.

Caffrey, B., Zhu, X., Berezuk, A., Tuttle, K., Chittori, S., and Subramaniam, S. (2021). AAA+ ATPase p97/VCP mutants and inhibitor binding disrupt inter-domain coupling and subsequent allosteric activation. J Biol Chem *297*.

Capo-Chichi, J.M., Boissel, S., Brustein, E., Pickles, S., Fallet-Bianco, C., Nassif, C., Patry, L., Dobrzeniecka, S., Liao, M., Labuda, D., *et al.* (2015). Disruption of CLPB is associated with congenital microcephaly, severe encephalopathy and 3-methylglutaconic aciduria. J Med Genet *52*, 303-311.

Chen, J., Noble, A.J., Kang, J.Y., and Darst, S.A. (2019a). Eliminating effects of particle adsorption to the air/water interface in single-particle cryo-electron microscopy: Bacterial RNA polymerase and CHAPSO. J Struct Biol X *1*.

Chen, X., Glytsou, C., Zhou, H., Narang, S., Reyna, D.E., Lopez, A., Sakellaropoulos, T., Gong, Y., Kloetgen, A., Yap, Y.S., *et al.* (2019b). Targeting Mitochondrial Structure Sensitizes Acute Myeloid Leukemia to Venetoclax Treatment. Cancer Discov *9*, 890-909.

Cooney, I., Han, H., Stewart, M.G., Carson, R.H., Hansen, D.T., Iwasa, J.H., Price, J.C., Hill, C.P., and Shen, P.S. (2019). Structure of the Cdc48 segregase in the act of unfolding an authentic substrate. Science *365*, 502-505.

Cupo, R.R., and Shorter, J. (2020). Skd3 (human ClpB) is a potent mitochondrial protein disaggregase that is inactivated by 3-methylglutaconic aciduria-linked mutations. Elife *9*.

Eisele, Y.S., Monteiro, C., Fearns, C., Encalada, S.E., Wiseman, R.L., Powers, E.T., and Kelly, J.W. (2015). Targeting protein aggregation for the treatment of degenerative diseases. Nat Rev Drug Discov *14*, 759-780.

Emsley, P., and Cowtan, K. (2004). Coot: model-building tools for molecular graphics. Acta Crystallogr D Biol Crystallogr *60*, 2126-2132.

Erzberger, J.P., and Berger, J.M. (2006). Evolutionary relationships and structural mechanisms of AAA+ proteins. Annu Rev Biophys Biomol Struct *35*, 93-114.

Evans, P.R. (2011). An introduction to data reduction: space-group determination, scaling and intensity statistics. Acta Crystallogr D Biol Crystallogr *67*, 282-292.

Fan, Y., Murgia, M., Linder, M.I., Mizoguchi, Y., Wang, C., Lyszkiewicz, M., Zietara, N., Liu, Y., Frenz, S., Sciuccati, G., *et al.* (2022). HAX1-dependent control of mitochondrial proteostasis governs neutrophil granulocyte differentiation. J Clin Invest *132*.

Fei, X., Bell, T.A., Jenni, S., Stinson, B.M., Baker, T.A., Harrison, S.C., and Sauer, R.T. (2020). Structures of the ATP-fueled ClpXP proteolytic machine bound to protein substrate. Elife *9*.

Frezza, C., Cipolat, S., and Scorrano, L. (2007). Organelle isolation: functional mitochondria from mouse liver, muscle and cultured fibroblasts. Nat Protoc *2*, 287-295.

Gao, H., Li, F., Ji, Z., Shi, Z., Li, Y., and Yu, H. (2022). Cryo-EM structures of human p97 double hexamer capture potentiated ATPase-competent state. Cell Discov *8*, 19.

Gates, S.N., and Martin, A. (2020). Stairway to translocation: AAA+ motor structures reveal the mechanisms of ATP-dependent substrate translocation. Protein Sci *29*, 407-419.

Gates, S.N., Yokom, A.L., Lin, J., Jackrel, M.E., Rizo, A.N., Kendsersky, N.M., Buell, C.E., Sweeny, E.A., Mack, K.L., Chuang, E., *et al.* (2017). Ratchet-like polypeptide translocation mechanism of the AAA+ disaggregase Hsp104. Science *357*, 273-279.

Grimminger-Marquardt, V., and Lashuel, H.A. (2010). Structure and function of the molecular chaperone Hsp104 from yeast.

Biopolymers *93*, 252-276.
Hoffmann, F.T., Kim, M., Beh, L.Y., Wang, J., Vo, P.L.H., Gelsinger, D.R., George, J.T., Acree, C., Mohabir, J.T., Fernandez, I.S., *et al.* (2022). Selective TnsC recruitment enhances the fidelity of RNA-guided transposition. Nature *609*, 384-393.
Hoq, M.R., Vago, F.S., Li, K., Kovaliov, M., Nicholas, R.J., Huryn, D.M., Wipf, P., Jiang, W., and Thompson, D.H. (2021). Affinity Capture of p97 with Small-Molecule Ligand Bait Reveals a 3.6 A Double-Hexamer Cryoelectron Microscopy Structure. ACS Nano *15*, 8376-8385.
Huang, D.W., Sherman, B.T., and Lempicki, R.A. (2009). Systematic and integrative analysis of large gene lists using DAVID bioinformatics resources. Nature Protocols *4*, 44-57.
Huang, D.W., Sherman, B.T., Tan, Q., Kir, J., Liu, D., Bryant, D., Guo, Y., Stephens, R., Baseler, M.W., Lane, H.C., *et al.* (2007). DAVID Bioinformatics Resources: expanded annotation database and novel algorithms to better extract biology from large gene lists. Nucleic Acids Res *35*, W169-175.
Huttlin, E.L., Bruckner, R.J., Navarrete-Perea, J., Cannon, J.R., Baltier, K., Gebreab, F., Gygi, M.P., Thornock, A., Zarraga, G., Tam, S., *et al.* (2021). Dual proteome-scale networks reveal cell-specific remodeling of the human interactome. Cell *184*, 3022-3040 e3028.
Jumper, J., Evans, R., Pritzel, A., Green, T., Figurnov, M., Ronneberger, O., Tunyasuvunakool, K., Bates, R., Zidek, A., Potapenko, A., *et al.* (2021). Highly accurate protein structure prediction with AlphaFold. Nature *596*, 583-589.
Kabsch, W. (2010). Xds. Acta Crystallogr D Biol Crystallogr *66*, 125-132.
Kanabus, M., Shahni, R., Saldanha, J.W., Murphy, E., Plagnol, V., Hoff, W.V., Heales, S., and Rahman, S. (2015). Bi-allelic CLPB mutations cause cataract, renal cysts, nephrocalcinosis and 3-methylglutaconic aciduria, a novel disorder of mitochondrial protein disaggregation. J Inherit Metab Dis *38*, 211-219.
Kater, L., Wagener, N., Berninghausen, O., Becker, T., Neupert, W., and Beckmann, R. (2020). Structure of the Bcs1 AAA-ATPase suggests an airlock-like translocation mechanism for folded proteins. Nat Struct Mol Biol *27*, 142-149.
Kim, G., Lee, S.G., Han, S.S., Jung, J., Jeong, H.S., Hyun, J.K., Rhee, D.K., Kim, H.M., and Lee, S. (2020). ClpL is a functionally active tetradecameric AAA plus chaperone, distinct from hexameric/dodecameric ones. Faseb J *34*, 14353-14370.
Kirstein, J., Moliere, N., Dougan, D.A., and Turgay, K. (2009). Adapting the machine: adaptor proteins for Hsp100/Clp and AAA+ proteases. Nat Rev Microbiol *7*, 589-599.
Kiykim, A., Garncarz, W., Karakoc-Aydiner, E., Ozen, A., Kiykim, E., Yesil, G., Boztug, K., and Baris, S. (2016). Novel CLPB mutation in a patient with 3-methylglutaconic aciduria causing severe neurological involvement and congenital neutropenia. Clin Immunol *165*, 1-3.
Lanzetta, P.A., Alvarez, L.J., Reinach, P.S., and Candia, O.A. (1979). An improved assay for nanomole amounts of inorganic phosphate. Anal Biochem *100*, 95-97.
Li, J., Mahajan, A., and Tsai, M.D. (2006). Ankyrin repeat: a unique motif mediating protein-protein interactions. Biochemistry *45*, 15168-15178.
Lo, Y.H., Sobhany, M., Hsu, A.L., Ford, B.L., Krahn, J.M., Borgnia, M.J., and Stanley, R.E. (2019). Cryo-EM structure of the essential ribosome assembly AAA-ATPase Rix7. Nat Commun *10*, 513.
Mastronarde, D.N. (2005). Automated electron microscope tomography using robust prediction of specimen movements. J Struct Biol *152*, 36-51.
McCoy, A.J., Grosse-Kunstleve, R.W., Adams, P.D., Winn, M.D., Storoni, L.C., and Read, R.J. (2007). Phaser crystallographic software. J Appl Crystallogr *40*, 658-674.
Miyata, T., Yamada, K., Iwasaki, H., Shinagawa, H., Morikawa, K., and Mayanagi, K. (2000). Two different oligomeric states of the RuvB branch migration motor protein as revealed by electron microscopy. J Struct Biol *131*, 83-89.

Mroz, D., Wyszkowski, H., Szablewski, T., Zawieracz, K., Dutkiewicz, R., Bury, K., Wortmann, S.B., Wevers, R.A., and Zietkiewicz, S. (2020). CLPB (caseinolytic peptidase B homolog), the first mitochondrial protein refoldase associated with human disease. Biochim Biophys Acta Gen Subj *1864*, 129512.

Olivares, A.O., Kotamarthi, H.C., Stein, B.J., Sauer, R.T., and Baker, T.A. (2017). Effect of directional pulling on mechanical protein degradation by ATP-dependent proteolytic machines. Proc Natl Acad Sci U S A *114*, E6306-E6313.

Pan, M., Yu, Y., Ai, H., Zheng, Q., Xie, Y., Liu, L., and Zhao, M. (2021). Mechanistic insight into substrate processing and allosteric inhibition of human p97. Nat Struct Mol Biol *28*, 614-625.

Pettersen, E.F., Goddard, T.D., Huang, C.C., Couch, G.S., Greenblatt, D.M., Meng, E.C., and Ferrin, T.E. (2004). UCSF Chimera--a visualization system for exploratory research and analysis. J Comput Chem *25*, 1605-1612.

Pettersen, E.F., Goddard, T.D., Huang, C.C., Meng, E.C., Couch, G.S., Croll, T.I., Morris, J.H., and Ferrin, T.E. (2021). UCSF ChimeraX: Structure visualization for researchers, educators, and developers. Protein Sci *30*, 70-82.

Pronicka, E., Ropacka-Lesiak, M., Trubicka, J., Pajdowska, M., Linke, M., Ostergaard, E., Saunders, C., Horsch, S., van Karnebeek, C., Yaplito-Lee, J.*, et al.* (2017). A scoring system predicting the clinical course of CLPB defect based on the foetal and neonatal presentation of 31 patients. J Inherit Metab Dis *40*, 853-860.

Puchades, C., Sandate, C.R., and Lander, G.C. (2020). The molecular principles governing the activity and functional diversity of AAA+ proteins. Nat Rev Mol Cell Biol *21*, 43-58.

Pudova, E.A., Krasnov, G.S., Kobelyatskaya, A.A., Savvateeva, M.V., Fedorova, M.S., Pavlov, V.S., Nyushko, K.M., Kaprin, A.D., Alekseev, B.Y., Trofimov, D.Y.*, et al.* (2020). Gene Expression Changes and Associated Pathways Involved in the Progression of Prostate Cancer Advanced Stages. Front Genet *11*, 613162.

Saita, S., Nolte, H., Fiedler, K.U., Kashkar, H., Venne, A.S., Zahedi, R.P., Kruger, M., and Langer, T. (2017). PARL mediates Smac proteolytic maturation in mitochondria to promote apoptosis. Nat Cell Biol *19*, 318-328.

Santo-Domingo, J., and Demaurex, N. (2012). Perspectives on: SGP symposium on mitochondrial physiology and medicine: the renaissance of mitochondrial pH. J Gen Physiol *139*, 415-423.

Santosh, V., Musayev, F.N., Jaiswal, R., Zarate-Perez, F., Vandewinkel, B., Dierckx, C., Endicott, M., Sharifi, K., Dryden, K., Henckaerts, E.*, et al.* (2020). The Cryo-EM structure of AAV2 Rep68 in complex with ssDNA reveals a malleable AAA(+) machine that can switch between oligomeric states. Nucleic Acids Research *48*, 12983-12999.

Saunders, C., Smith, L., Wibrand, F., Ravn, K., Bross, P., Thiffault, I., Christensen, M., Atherton, A., Farrow, E., Miller, N.*, et al.* (2015). CLPB variants associated with autosomal-recessive mitochondrial disorder with cataract, neutropenia, epilepsy, and methylglutaconic aciduria. Am J Hum Genet *96*, 258-265.

Sherman, B.T., Hao, M., Qiu, J., Jiao, X., Baseler, M.W., Lane, H.C., Imamichi, T., and Chang, W. (2022). DAVID: a web server for functional enrichment analysis and functional annotation of gene lists (2021 update). Nucleic Acids Res.

Soto, C., and Pritzkow, S. (2018). Protein misfolding, aggregation, and conformational strains in neurodegenerative diseases. Nat Neurosci *21*, 1332-1340.

Tang, W.K., Borgnia, M.J., Hsu, A.L., Esser, L., Fox, T., de Val, N., and Xia, D. (2020). Structures of AAA protein translocase Bcs1 suggest translocation mechanism of a folded protein. Nat Struct Mol Biol *27*, 202-209.

Terwilliger, T.C., Grosse-Kunstleve, R.W., Afonine, P.V., Moriarty, N.W., Zwart, P.H., Hung, L.W., Read, R.J., and Adams, P.D. (2008). Iterative model building, structure refinement and density modification with the PHENIX AutoBuild wizard. Acta Crystallogr D Biol Crystallogr *64*, 61-69.

Thevarajan, I., Zolkiewski, M., and Zolkiewska, A. (2020). Human CLPB forms ATP-dependent complexes in the mitochondrial intermembrane space. Int J Biochem Cell Biol *127*, 105841.

Twomey, E.C., Ji, Z., Wales, T.E., Bodnar, N.O., Ficarro, S.B., Marto, J.A., Engen, J.R., and Rapoport, T.A. (2019). Substrate

processing by the Cdc48 ATPase complex is initiated by ubiquitin unfolding. Science *365*.

Wakula, M., Balcerak, A., Rubel, T., Chmielarczyk, M., Konopinski, R., Lyczek, F., and Grzybowska, E.A. (2020). The interactome of multifunctional HAX1 protein suggests its role in the regulation of energy metabolism, de-aggregation, cytoskeleton organization and RNA-processing. Biosci Rep *40*.

Warren, J.T., Cupo, R.R., Wattanasirakul, P., Spencer, D.H., Locke, A.E., Makaryan, V., Bolyard, A.A., Kelley, M.L., Kingston, N.L., Shorter, J.*, et al.* (2022). Heterozygous variants of CLPB are a cause of severe congenital neutropenia. Blood *139*, 779-791.

Weaver, C.L., Duran, E.C., Mack, K.L., Lin, J., Jackrel, M.E., Sweeny, E.A., Shorter, J., and Lucius, A.L. (2017). Avidity for Polypeptide Binding by Nucleotide-Bound Hsp104 Structures. Biochemistry *56*, 2071-2075.

Wortmann, S.B., Zietkiewicz, S., Guerrero-Castillo, S., Feichtinger, R.G., Wagner, M., Russell, J., Ellaway, C., Mroz, D., Wyszkowski, H., Weis, D.*, et al.* (2021). Neutropenia and intellectual disability are hallmarks of biallelic and de novo CLPB deficiency. Genet Med *23*, 1705-1714.

Wortmann, S.B., Zietkiewicz, S., Kousi, M., Szklarczyk, R., Haack, T.B., Gersting, S.W., Muntau, A.C., Rakovic, A., Renkema, G.H., Rodenburg, R.J.*, et al.* (2015). CLPB mutations cause 3-methylglutaconic aciduria, progressive brain atrophy, intellectual disability, congenital neutropenia, cataracts, movement disorder. Am J Hum Genet *96*, 245-257.

Yu, G., Bai, Y., Li, K., Amarasinghe, O., Jiang, W., and Zhang, Z.Y. (2021). Cryo-electron microscopy structures of VCP/p97 reveal a new mechanism of oligomerization regulation. iScience *24*, 103310.

Yu, X., VanLoock, M.S., Poplawski, A., Kelman, Z., Xiang, T., Tye, B.K., and Egelman, E.H. (2002). The Methanobacterium thermoautotrophicum MCM protein can form heptameric rings. Embo Rep *3*, 792-797.

Zhang, K. (2016). Gctf: Real-time CTF determination and correction. J Struct Biol *193*, 1-12.

Zheng, S.Q., Palovcak, E., Armache, J.P., Verba, K.A., Cheng, Y., and Agard, D.A. (2017). MotionCor2: anisotropic correction of beam-induced motion for improved cryo-electron microscopy. Nat Methods *14*, 331-332.

Zivanov, J., Nakane, T., and Scheres, S.H.W. (2020). Estimation of high-order aberrations and anisotropic magnification from cryo-EM data sets in RELION-3.1. IUCrJ *7*, 253-267.

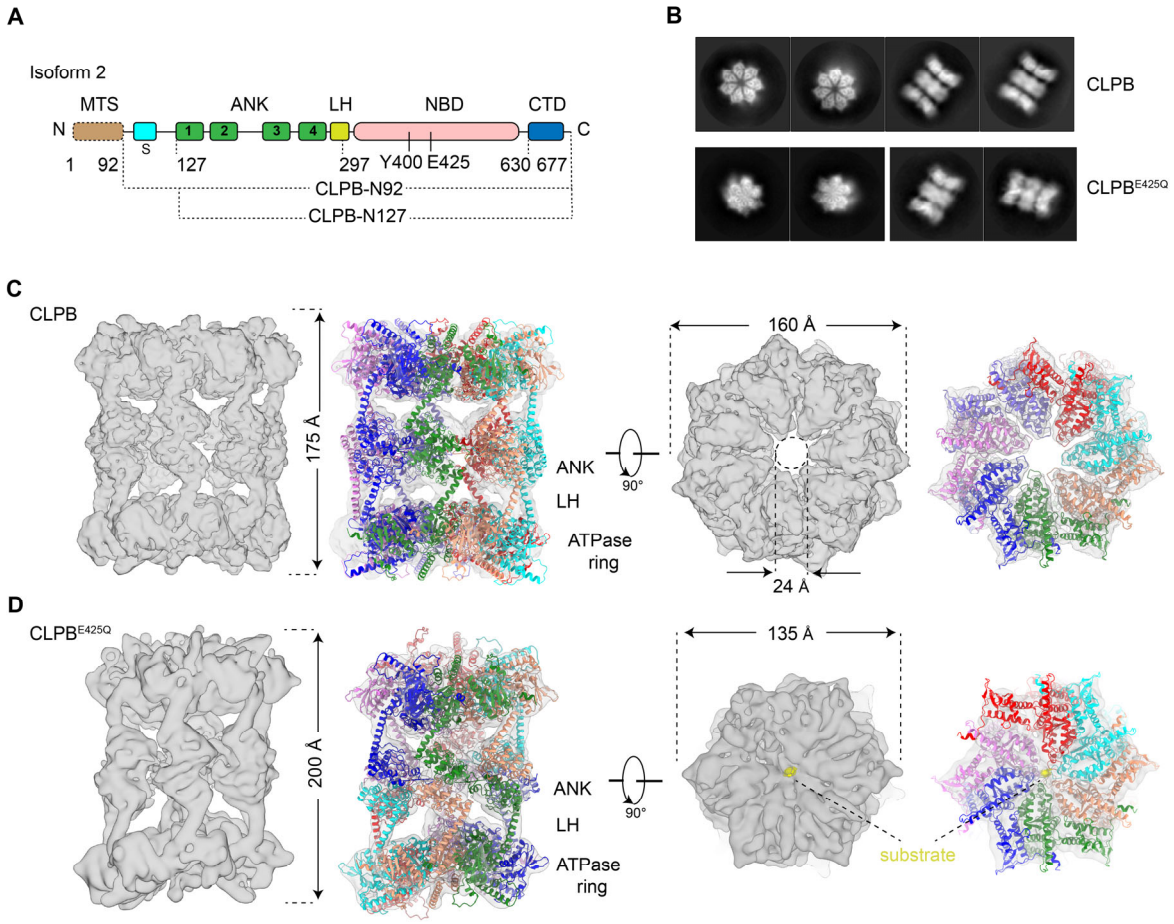

Figure 1. Cryo-EM structures of CLPB double-heptamers in the apo-state and CLPB^{E425Q} double-hexamers in the substrate-bound state.

A Domain organization of *H. sapiens* CLPB. CLPB is composed of an MTS, a short hydrophobic stretch (S), a linker helix (LH), four ankyrin-repeat (ANK) motifs, an NBD, and a CTD.

B Representative 2D classification averages of CLPB and CLPB^{E425Q} datasets.

C, **D** The density maps of the double-heptamer (C) and double-hexamer (D), superimposed with the models of CLPB. The density maps are shown in the side and top (ATPase ring) views. The higher-order oligomer is mediated by ANK domains. LH, linker helix. The substrate was labelled as yellow.

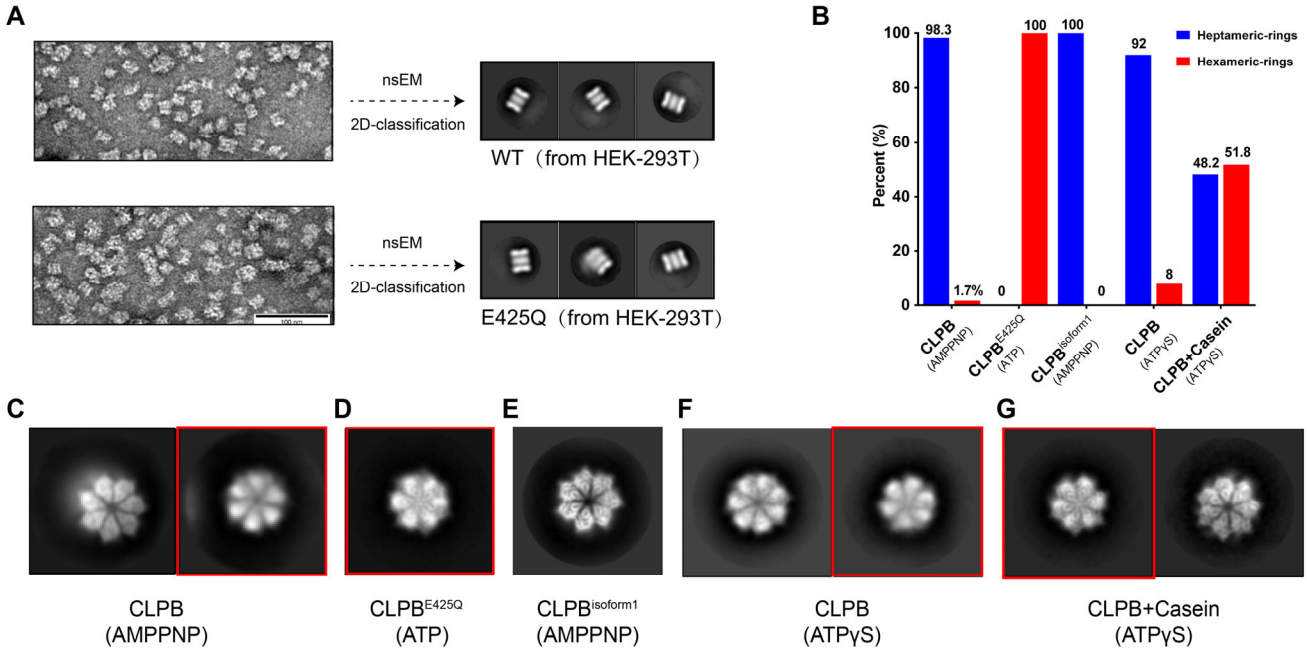

Figure 2. The CLPB double-heptamers transform into double-hexamers upon substrate binding.
A CLPB complexes purified from HEK293 cells form double oligomeric state. Representative nsEM images (left) and 2D classification averages of nsEM particles (right) of CLPB and CLPB^{E425Q} from HEK-293T cells.
B The proportion of the hexameric and heptameric top views in the CLPB-AMPPNP, CLPB^{E425Q}-ATP, CLPB^{isoform1}-AMPPNP, CLPB-ATPγs and CLPB+Casein-ATPγs datasets.
C-G Representative top views of 2D classification averages of CLPB-AMPPNP (C), CLPB^{E425Q}-ATP (D), CLPB^{isoform1}-AMPPNP (E), CLPB-ATPγs (F) and CLPB+Casein-ATPγs (G) datasets. The top views with hexameric feature are indicated by red boxes.

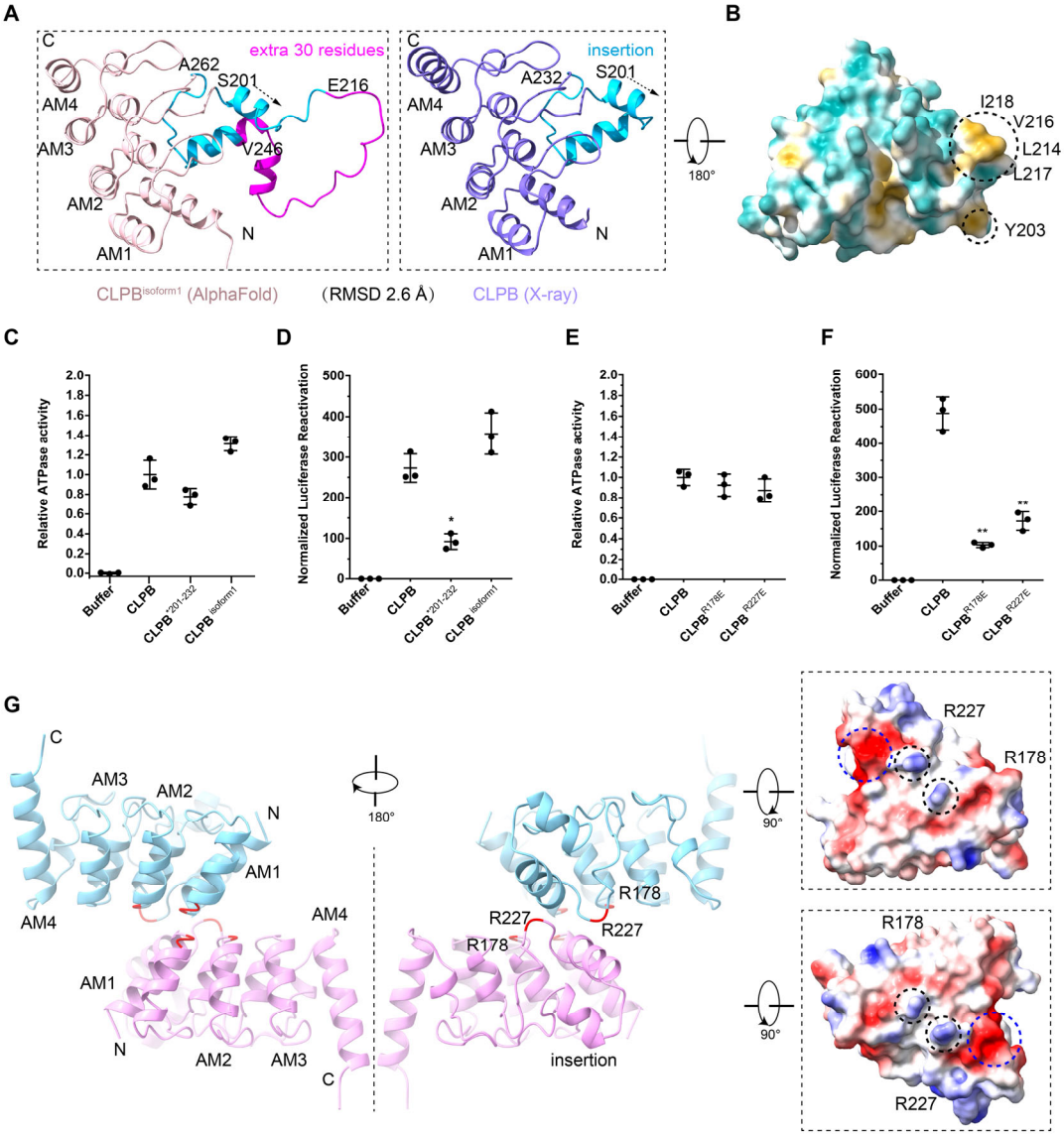

Figure 3. ANK domain is essential for the disaggregase activity of CLPB.

A X-ray crystallography structure and AlphaFold predicted model of the ANK domain. The RMSD between these two structures is 2.6 Å.

B The hydrophobic surfaces of the ANK domain. Two hydrophobic patches were found in the unique insertion.

C The ATPase assay of CLPB, CLPB$^{\Delta 201\text{-}232}$ and CLPB^{isoform1}. ATPase activity was compared to CLPB (N=3, individual data points shown as dots, bars show mean ± SD).

D The disaggregase activity assay of CLPB, CLPB$^{\Delta 201\text{-}232}$ and CLPB^{isoform1}. Disaggregase activity was compared to CLPB (N=3, individual data points shown as dots, bars show mean ± SD, *p<0.05).

E ATPase assay of CLPB, CLPB^{R178E} and CLPB^{R227E}.

F Disaggregase activity assay of CLPB, CLPB^{R178E} and CLPB^{R227E}. Results show that the disaggregase activities of CLPB^{R178E} and CLPB^{R227E} are reduced by 70-80% (N=3, individual data points shown as dots, bars show mean ± SD, **p<0.01).

G The ANK domain dimer interface. One is the AM1-AM2 and the other is the second helix of the insertion. Two positive residues (R178 and R227) are outstanding in the ANK surface electrostatic potential.

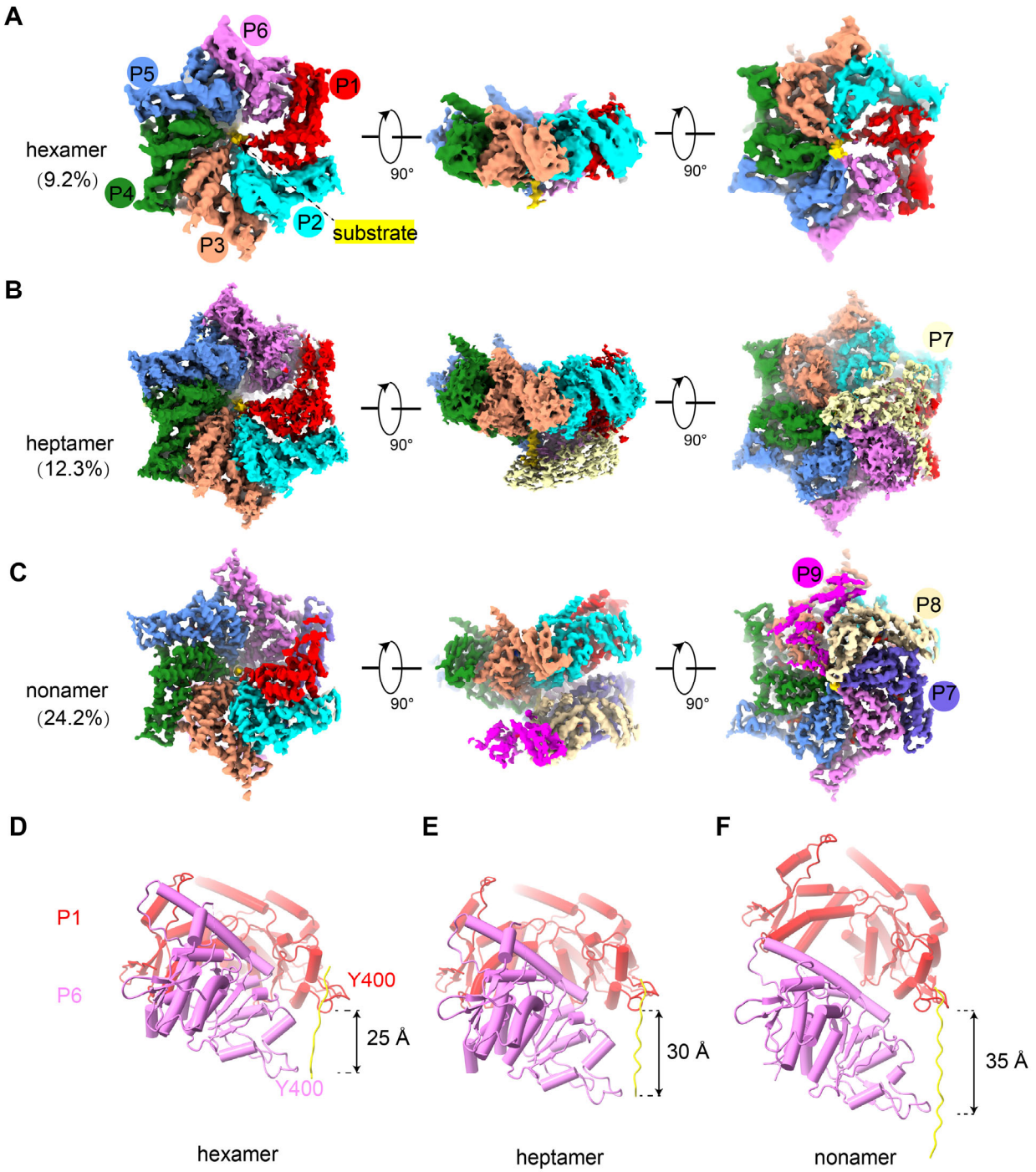

Figure 4. Cryo-EM characterization of the NBD helical structures of CLPB.

A-C Density maps of the NBD hexamer (A), heptamer (B) and nonamer (C), respectively. Protomers are painted in different colors.

D-F Distances along the central substrate between the pore-loop residue Y400 of P1 and P6 in the hexamer (D), heptamer (E) and nonamer (F). The axial rise of P6 relatively to P1 are labelled.

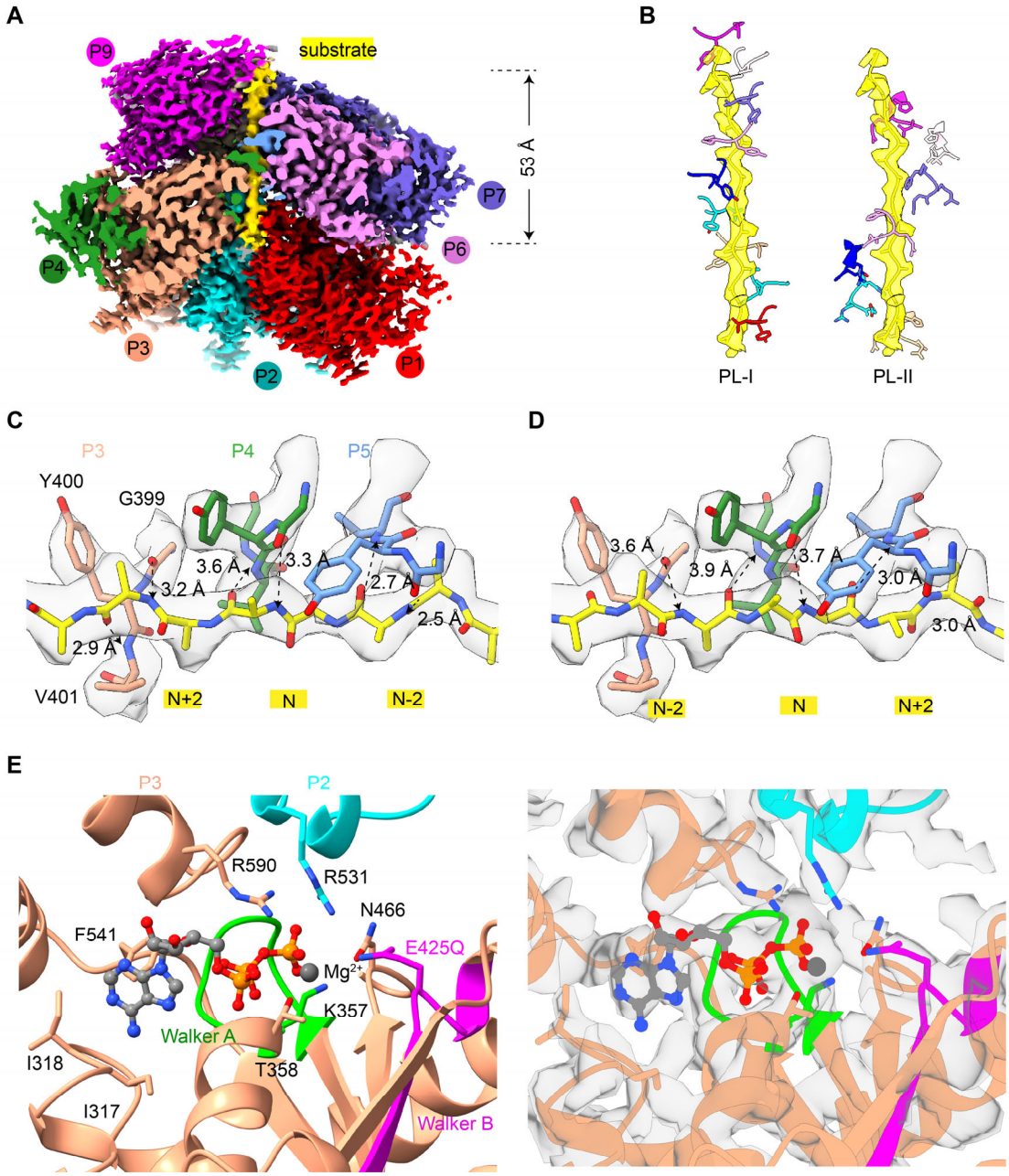

Figure 5. Structure of the NBD nonamer in processing a peptide substrate.

A Density map of the NBD nonamer in the substrate-processing state. Nine protomers are indicated as P1 to P9 and painted in different colors. The central substrate is colored yellow.

B The spiral configuration of the PLs of CLPB protomers around the substrate in the central channel. PL-Is and PL-IIs are shown in the left and right panels, respectively. While the conserved PL-Is (G399-Y400-V401-G402) directly interact with the substrate, the PL-IIs (E386-R387-H388) situate in slightly larger distances from the substrate.

C, D Magnified view of the interactions between the PL-I of P3, P4 and P5 and the backbone of substrate. The substrate could be modeled in both directions, N to C or C to N. The potential hydrogen bonds are indicated by

dashed lines and the distances are labelled.

E Magnified view of the conserved ATP-binding pocket of CLPB. Functionally important residues of Walker A motif (K357, T358), Walker B motif (E425), sensor-1 (N466), sensor-2 (R590), arginine finger (R531) and the conserved residue I317, I318. Atomic model and density map are shown in the left and right panels, respectively.

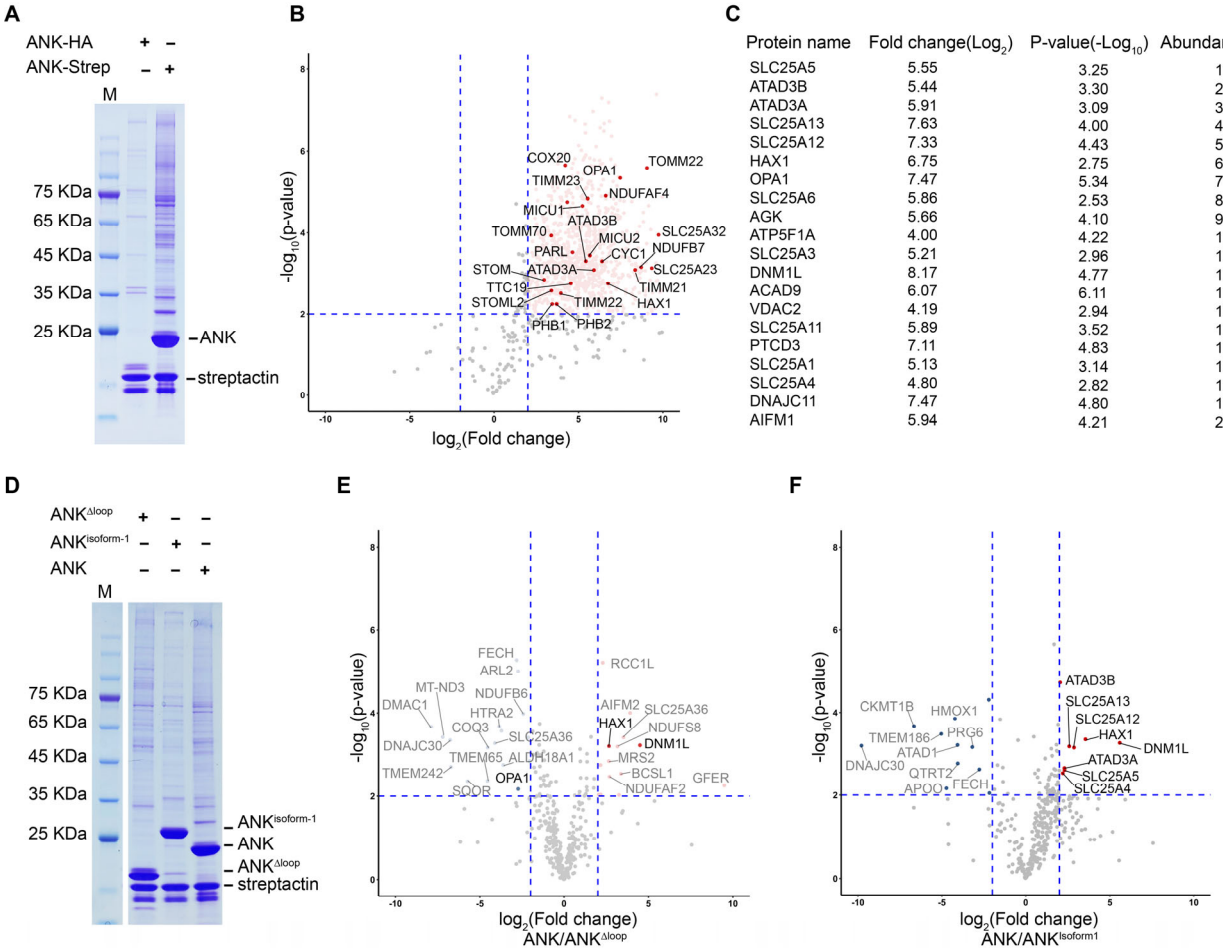

Figure 6. The mitochondrial interactome of the ANK domain.

A HEK-293F cells expressing the MTS-ANK-HA or MTS-ANK-Strep constructs were subjected to anti-Strep immunoprecipitation. Precipitates were analyzed by SDS-PAGE, Coomassie blue staining and mass-spectrometry (MS).

B Volcano plot showing the mitochondrial proteins co-precipitated with MTS-ANK-Strep. 934 proteins that were more enriched in the MTS-ANK-Strep are labelled in light red. The potential substrates, previously reported to be most affected by *CLPB*-knockout, are highlighted in red. A relatively stringent criterion (fold-change > 4 and p-value < 0.01) were used for enrichment analysis (three biological replicates), indicating with blue dashed lines.

C Top-20 proteins in OM, IMS and IM are listed, based on the ranking of protein abundances.

D HEK-293F cells expressing the MTS-ANK-Strep, MTS-ANK$^{\Delta loop}$-Strep and MTS-ANK^{isoform1}-Strep constructs were subjected to anti-Strep immunoprecipitation. Precipitates were analyzed by SDS-PAGE, Coomassie blue staining and MS.

E, F Volcano plot showing the fold change of the OM, IMS and IM mitochondrial proteins in MTS-ANK-Strep compared to MTS-ANK$^{\Delta loop}$-Strep (E) or MTS-ANK^{isoform1}-Strep (F). Proteins in the top-20 list (C) were highlighted in red.

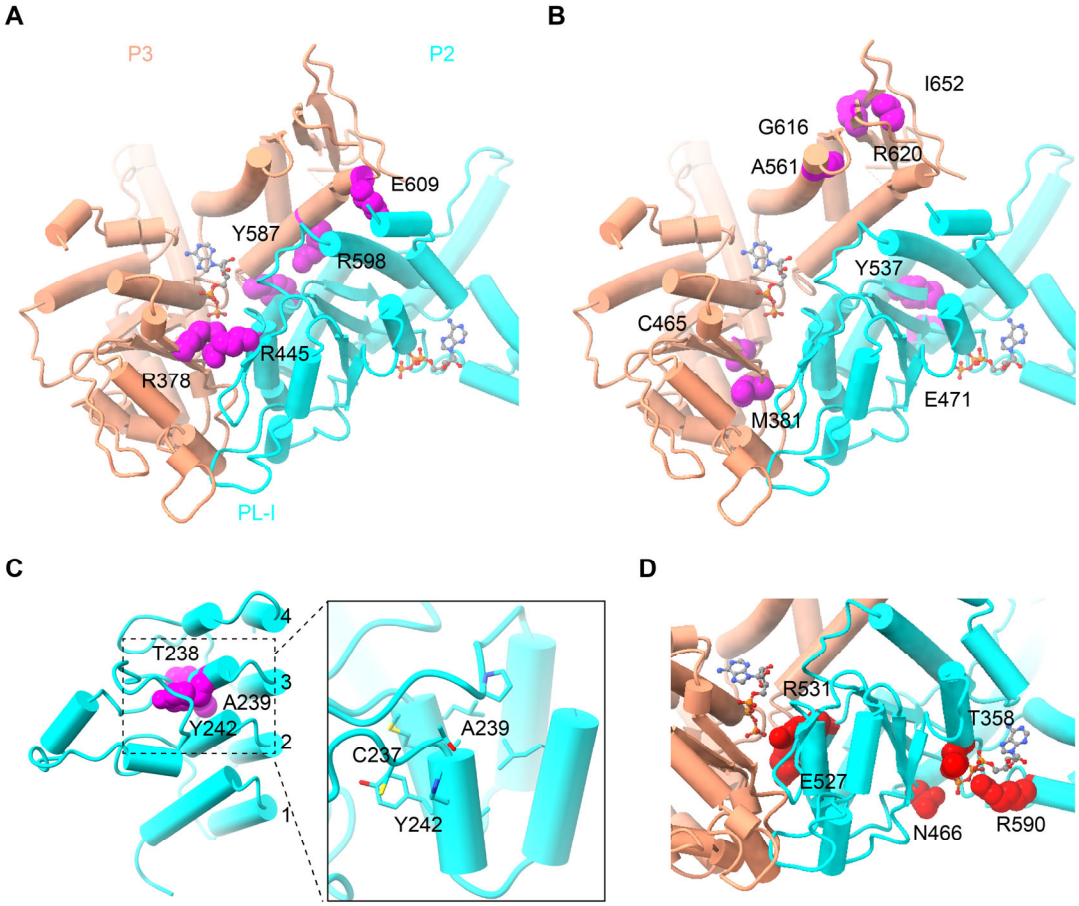

Figure 7. The disease-related mutations of CLPB in 3-MGA and SCN.

A 3-MGA-related mutations in the interface of adjacent protomers.

B 3-MGA-related mutations within the large and small subdomain of the ATPase domain.

C 3-MGA-related mutations in the ANK domain.

D SCN-related mutations in the ATP-binding pocket. Residues on the positions of these mutation are highlighted in magenta or red sphere models. ATP molecule is highlighted in stick models.

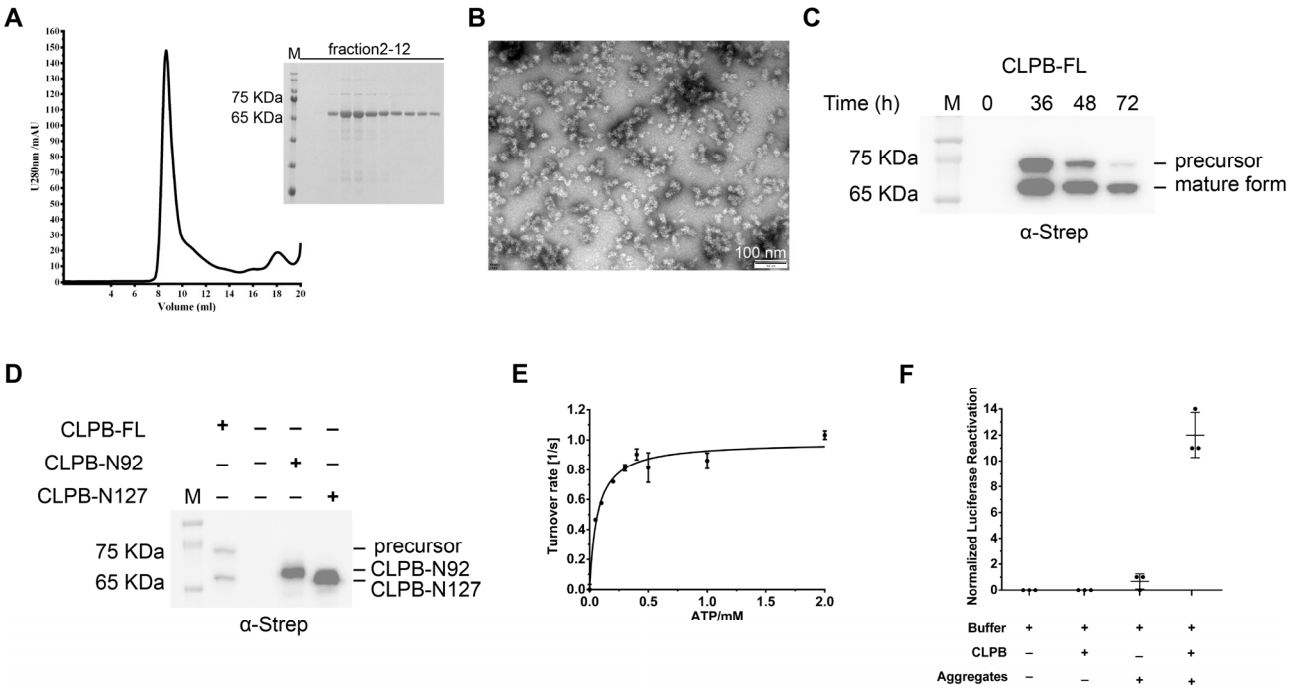

S1. Biochemical and functional characterization of CLPB proteins.

A The purification of CLPB-N92, analyzing by size-exclusion chromatography (left) and SDS-PAGE (right).

B Negative staining electron microscopy (nsEM) of the peak fraction in (A). Result shows that CLPB-N92 formed large aggregates and was highly heterogenous in size.

C Time course of the C-terminal Step-tagged full-length CLPB (CLPB-FL) expression in transiently transfected HEK-293T cells.

D CLPB-FL, CLPB-N92 and CLPB-N127 expression in transiently transfected HEK-293T cells. Data show that the CLPB-N127 has the same molecular weight as the mature form of CLPB.

E ATPase activity of CLPB-N127.

F Disaggregase activity of CLPB-N127.

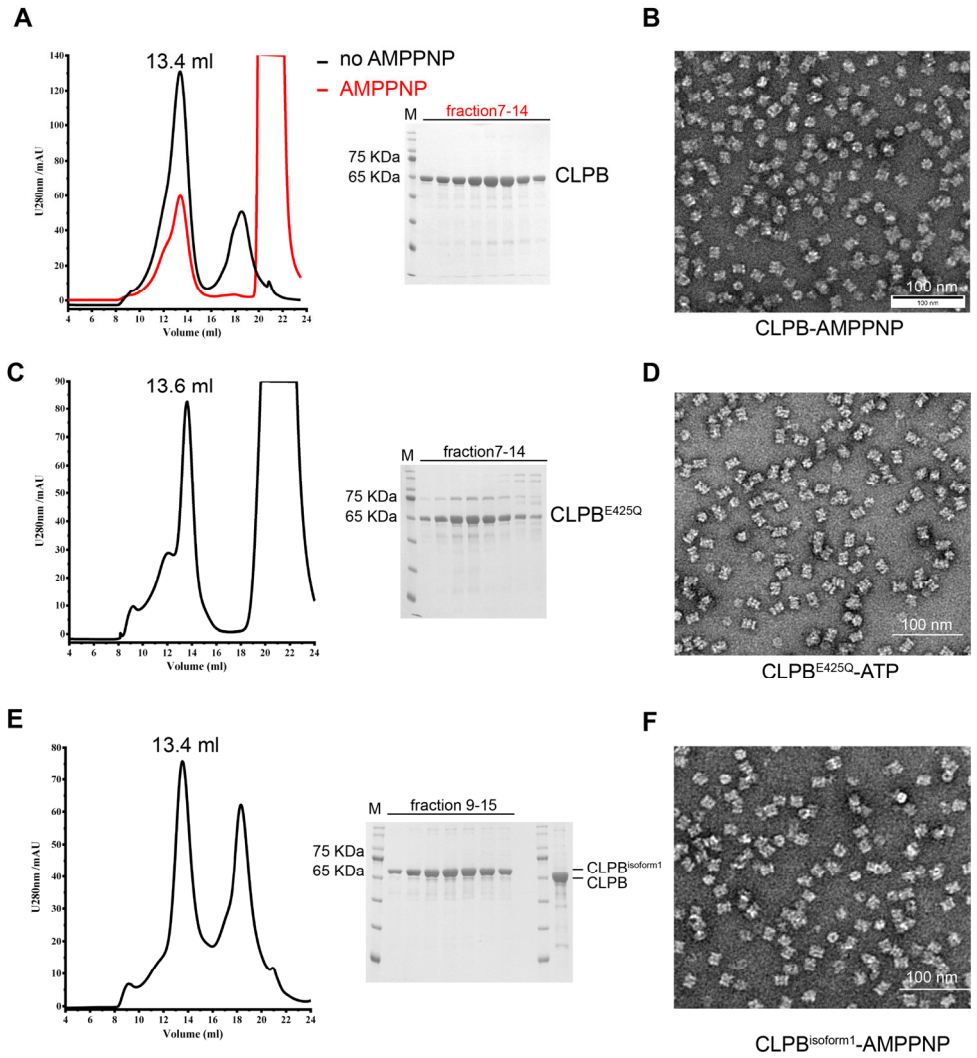

S2. Sample preparation of CLPB-AMPPNP, CLPB^{E425Q}-ATP and CLPB^{isoform1}-AMPPNP.

A Purification of CLPB using size-exclusion chromatography with AMPPNP (red line) or without AMPPNP (black line). Corresponding fractions were analyzed by SDS-PAGE (right panel).

B Representative nsEM image of the peak fraction in (A).

C Purification of CLPB^{E425Q} using size-exclusion chromatography in the presence of ATP. Corresponding fractions were analyzed by SDS-PAGE (right panel).

D Representative nsEM image of the peak fraction in (C).

E Purification of CLPB^{isodorm1} using size-exclusion chromatography. Corresponding fractions were analyzed by SDS-PAGE (right panel).

F Representative nsEM image of the peak fraction in (E)

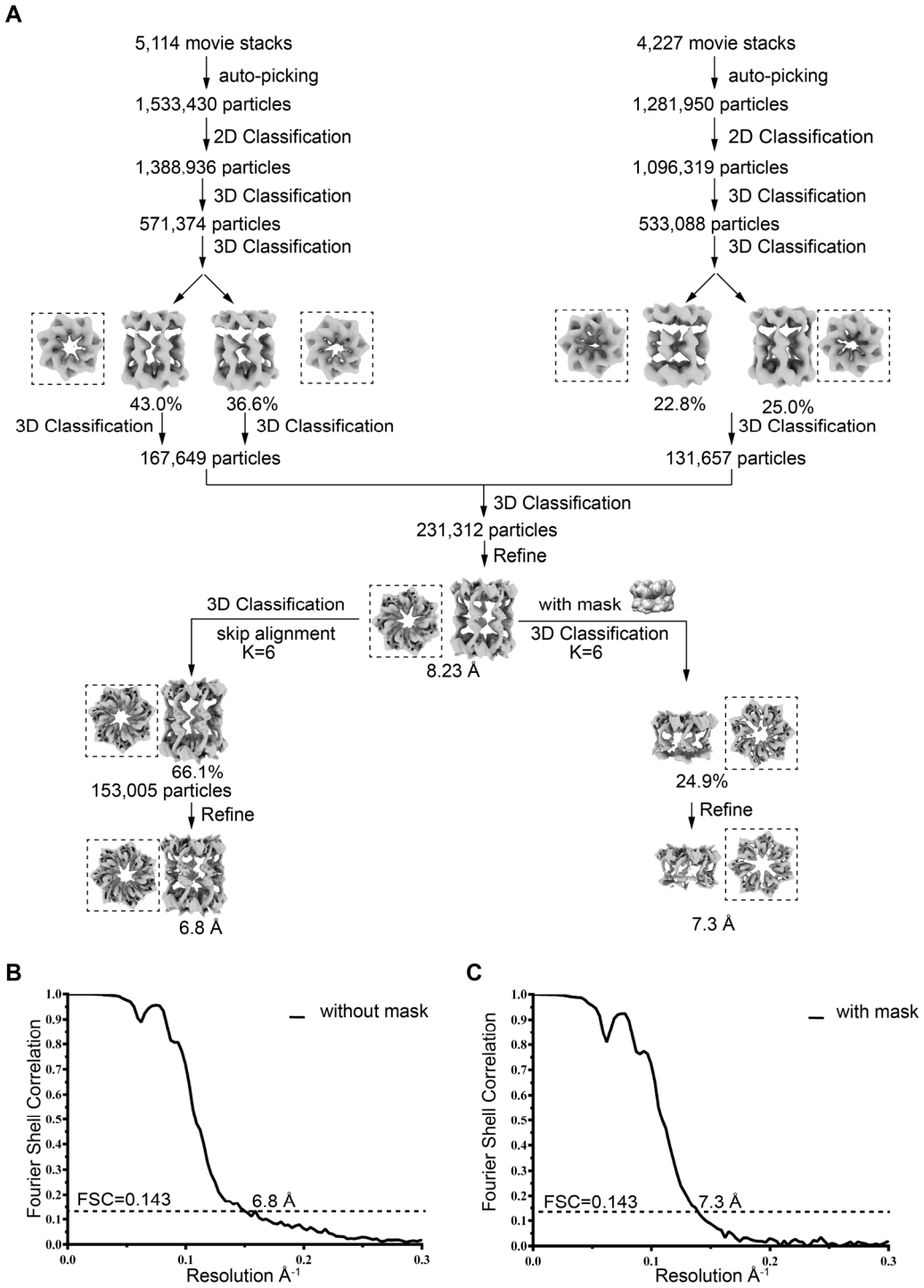

S3. Image processing workflow of the CLPB-AMPPNP dataset.

A Image processing workflow of the CLPB dataset (see Methods for details).

B, C Fourier Shell Correlation (FSC) curves for the final cryo-EM map of the double-heptameric complex (B) or heptameric complex (C) using the gold standard FSC 0.143 criteria.

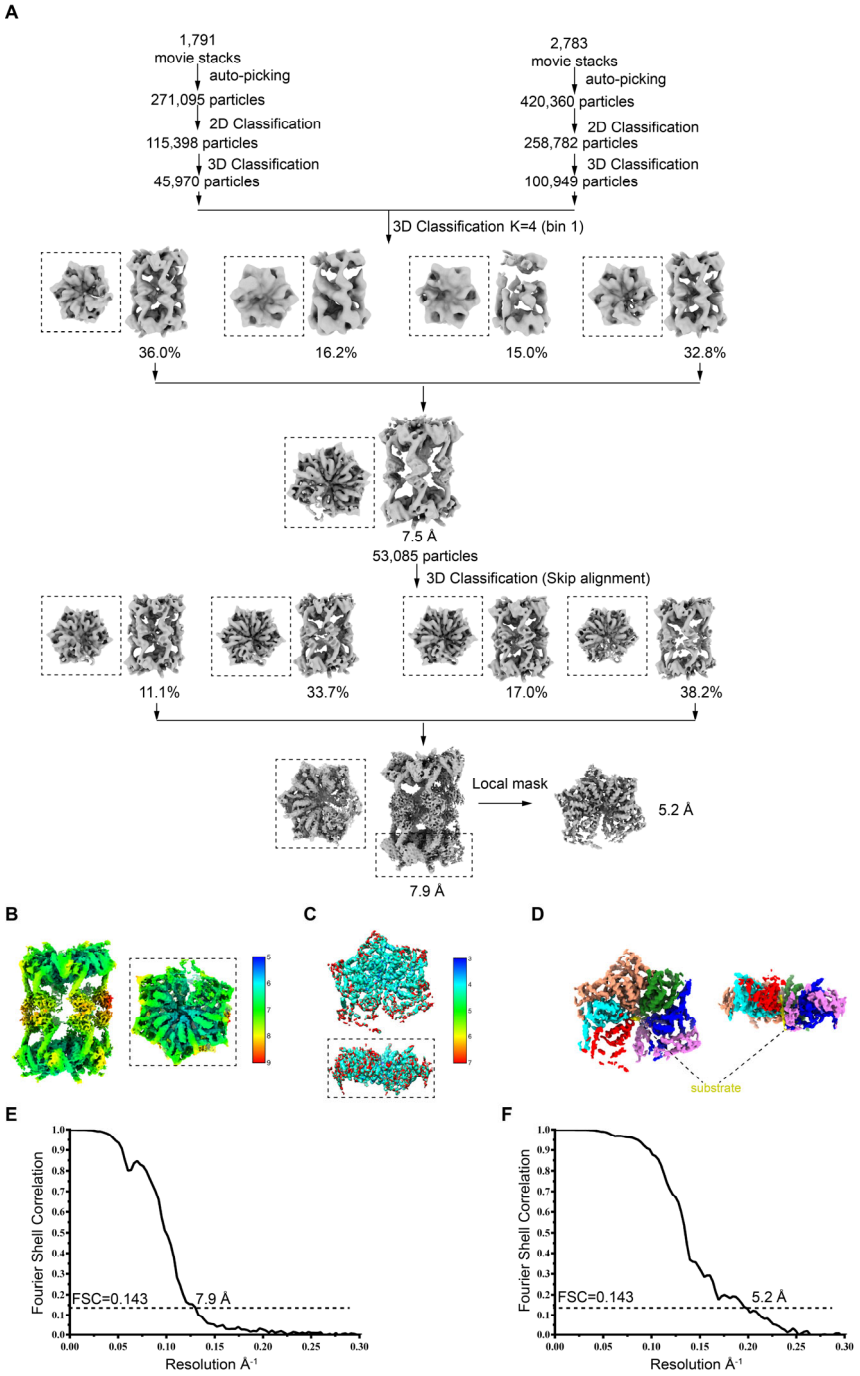

S4. Image processing workflow of the CLPB^{E425Q}-ATP dataset.

A Image processing workflow of the CLPB^{E425Q} dataset.

B, C Local resolution estimation of CLPB^{E425Q} double-hexamer (B) or NBD alone (C).

D Density map of the NBD alone. The central substrate is colored yellow.

E, F Fourier shell correlation (FSC) curve of the final map of the CLPB^{E425Q} double-hexamer (E) and NBD (F).

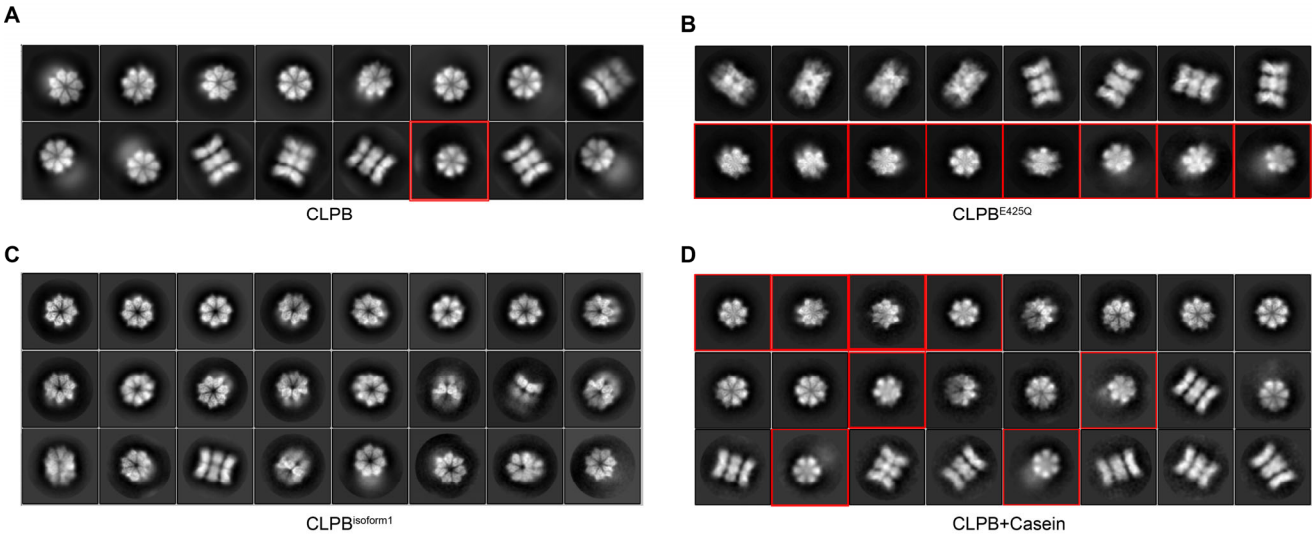

S5. Conversion of the CLPB double-heptamer to double-hexamer upon substrate binding.
A-D Representative 2D classification averages of CLPB (A), CLPB^{E425Q} (B), CLPB^{isoform1} (C) and CLPB+Casein (D) datasets. The top views with hexameric features are indicated by red boxes.

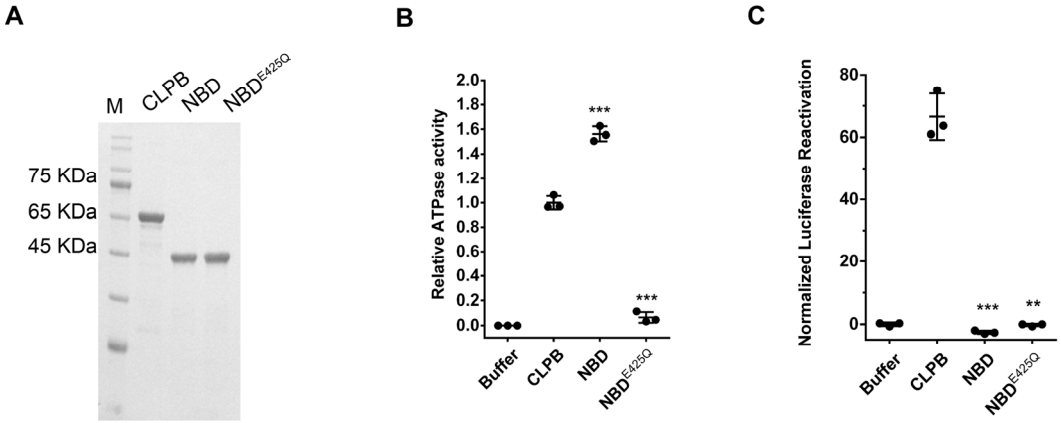

S6. The ANK domain is essential for the disaggregase activity of CLPB.

A SDS-PAGE analysis of the purified proteins.

B ATPase assays of CLPB, NBD and NBD^{E425Q}. Results show that NBD^{E425Q} has nearly no ATPase activity. NBD has strong ATPase activity. ATPase activity was compared to CLPB (N=3, individual data points shown as dots, bars show mean ± SD, *p<0.05, **p<0.01, ***p<0.0001).

C Disaggregase activity assay of CLPB, NBD and NBD^{E425Q}. The results show that NBD and NBD^{E425Q} abolish the disaggregase activity of CLPB. Disaggregase activity was compared to CLPB (N=3, individual data points shown as dots, bars show mean ± SD, **p<0.01, ***p<0.0001).

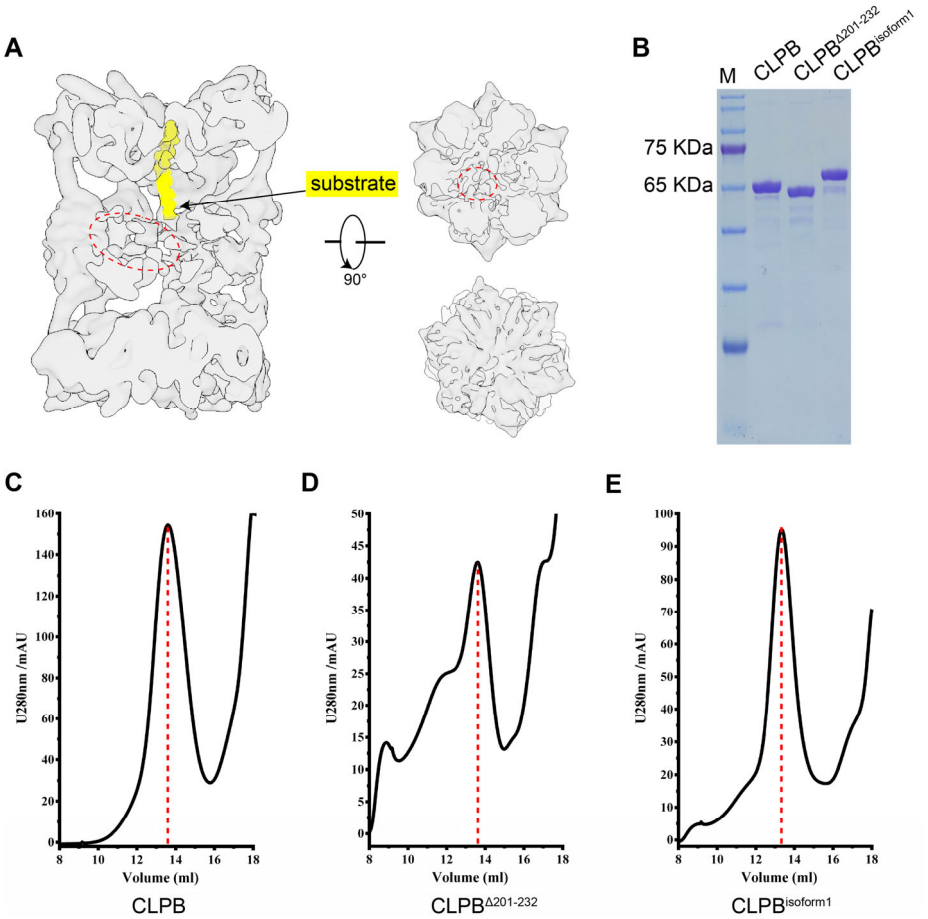

S7. The unique insertion in ANK domain mediates higher-order structure formation and directly contact the substrate.

A Residual densities around the ANK domains, extending towards the central channel of the CLPB^{E425Q} complex in the substrate-bound state. The extra densities are highlighted by a dotted ellipse. The density of the substrate is shown in yellow.

B SDS-PAGE analysis of the purified proteins.

C-E Purification of CLPB, CLPB$^{\Delta 201\text{-}232}$ and CLPB^{isoform1} complexes using size-exclusion chromatography.

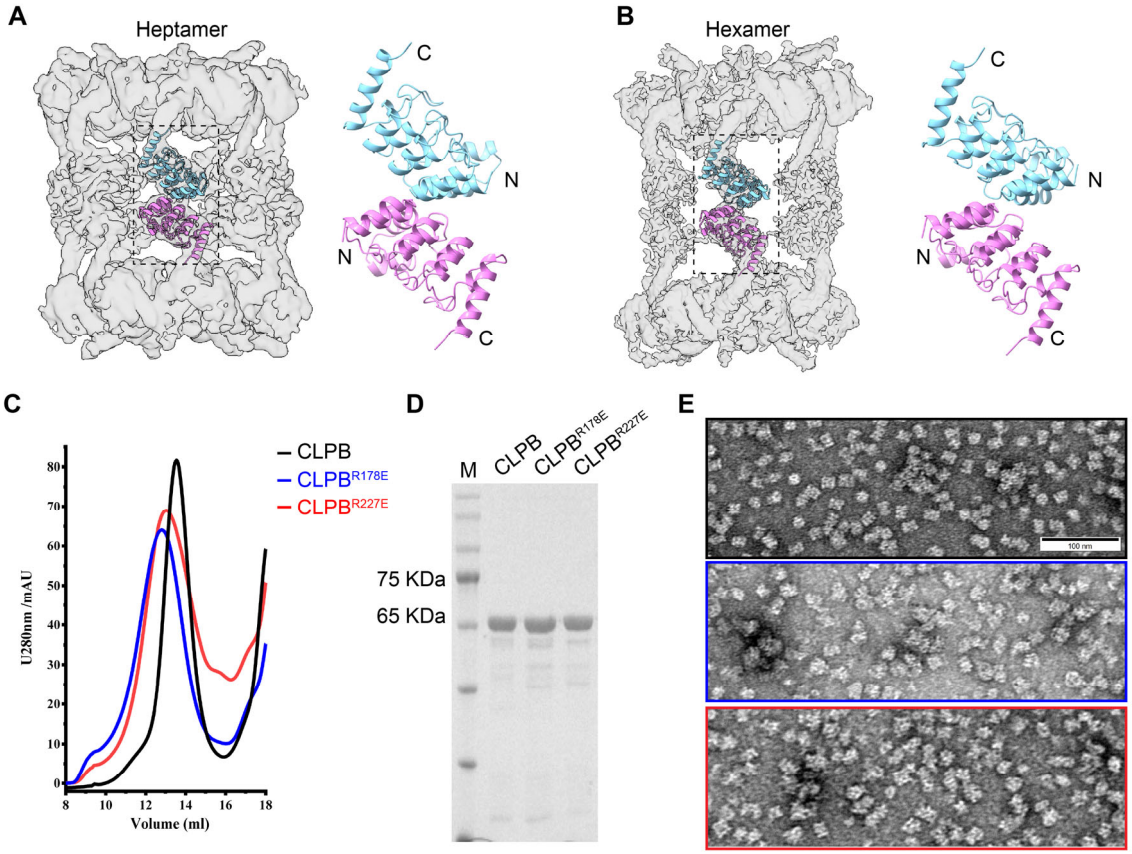

S8. The ANK domain dimer interface in the double-heptamer and double-hexamer

A, B Rigid-body fitting of the crystal structure of the ANK domain into the density maps of the double-heptamer (A) and double-hexamer (B).

C Purification of the CLPB, CLPB^{R178E} and CLPB^{R227E} complexes using size-exclusion chromatography.

D SDS-PAGE analysis of the purified proteins.

E Representative nsEM images of the CLPB (black line rectangle), CLPB^{R178E} (blue line rectangle) and CLPB^{R227E} complexes (red line rectangle).

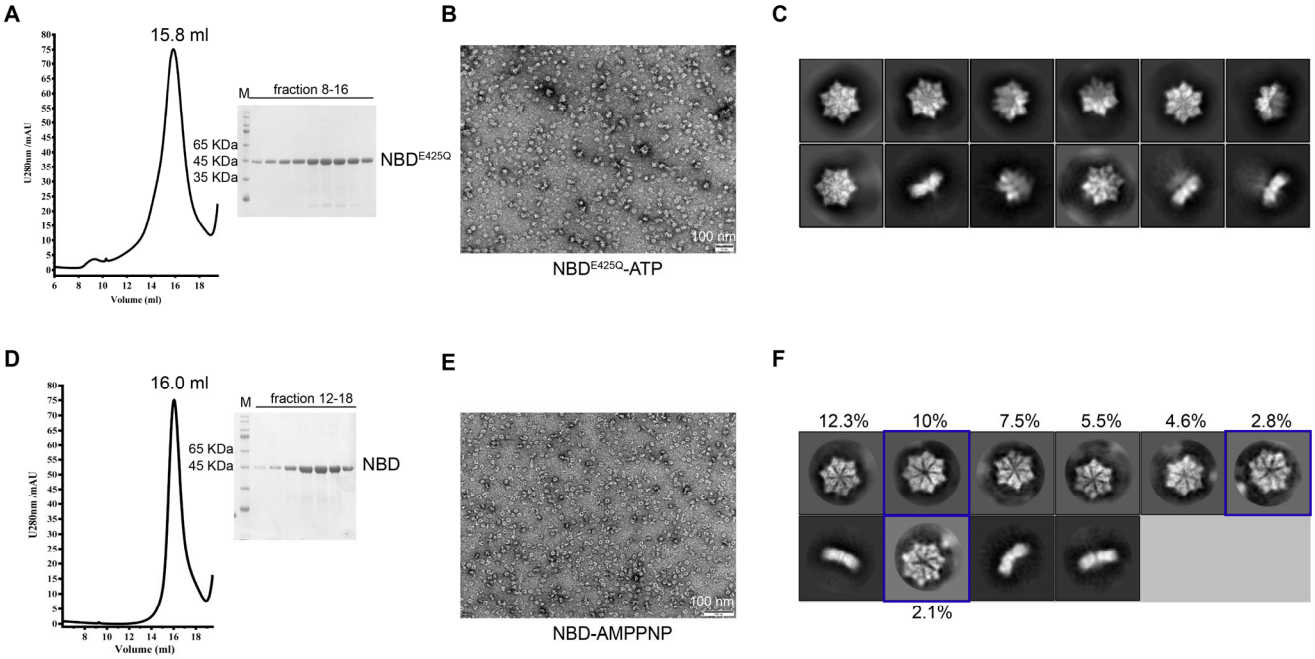

S9. Sample preparation of the NBD^{E425Q}-ATPand NBD-AMPPNP complex.

A Purification of NBD^{E425Q} using size-exclusion chromatography in the presence of ATP. Corresponding fractions were analyzed by SDS-PAGE

B, C Representative nsEM image (B) and cryo-EM 2D classification averages (C) of the peak fraction in (A).

D Purification of NBD using size-exclusion chromatography in the presence of AMPPNP. Corresponding fractions were analyzed by SDS-PAGE (right panel).

E, F Representative nsEM image (E) and cryo-EM 2D classification averages (F) of the peak fraction in (D). The hexameric ring is more compact than hepatameric ring, and the diameter of central pore of hexamer is much smaller than that of heptamer.

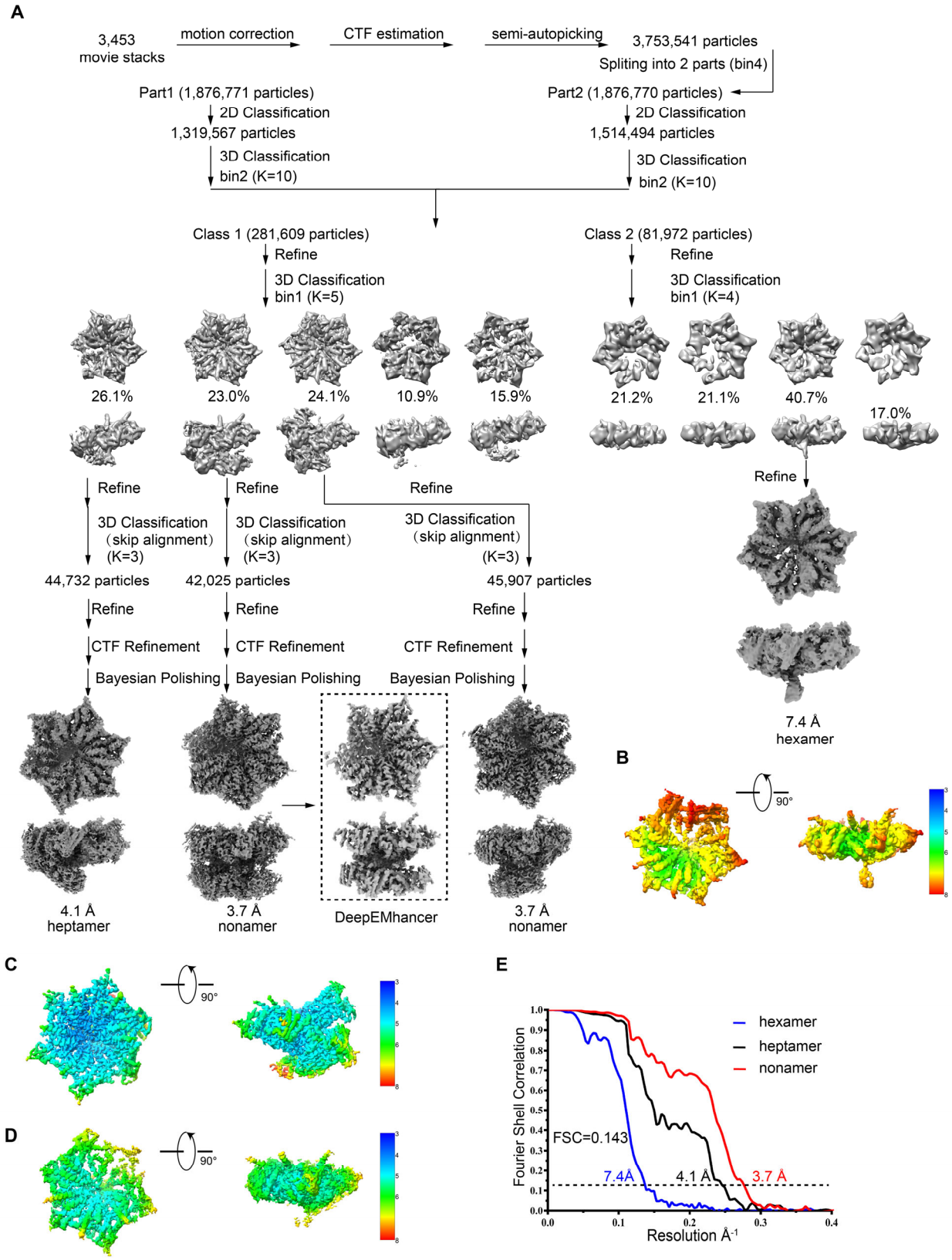
A
3,453
movie stacks
motion correction
CTF estimation
semi-autopicking
3,753,541 particles
Spliting into 2 parts (bin4)
Part1 (1,876,771 particles)
2D Classification
1,319,567 particles
3D Classification
bin2 (K=10)
Part2 (1,876,770 particles)
2D Classification
1,514,494 particles
3D Classification
bin2 (K=10)
Class 1 (281,609 particles)
Refine
3D Classification
bin1 (K=5)
Class 2 (81,972 particles)
Refine
3D Classification
bin1 (K=4)
26.1%
23.0%
24.1%
10.9%
15.9%
21.2%
21.1%
40.7%
17.0%
Refine
Refine
Refine
Refine
3D Classification
(skip alignment)
(K=3)
3D Classification
(skip alignment)
(K=3)
3D Classification
(skip alignment)
(K=3)
44,732 particles
42,025 particles
45,907 particles
Refine
Refine
Refine
CTF Refinement
CTF Refinement
CTF Refinement
Bayesian Polishing
Bayesian Polishing
Bayesian Polishing
7.4 Å
hexamer
4.1 Å
heptamer
3.7 Å
nonamer
DeepEMhancer
3.7 Å
nonamer
B
90°
C
90°
D
90°
E
Fourier Shell Correlation
Resolution Å-1
hexamer
heptamer
nonamer
FSC=0.143
7.4Å
4.1 Å
3.7 Å

889

S10. Image processing workflow of the NBD^{E425Q} dataset.

A Image processing workflow of the NBD^{E425Q} dataset. The micrographs were subjected to motion correction and CTF estimation. The auto-picked particles were subjected to multiple rounds of 2D and 3D classifications. Three different oligomeric arrangements, hexameric, heptameric and nonameric were identified.

B-D Local resolution estimation of the density maps of the hexamer (B), heptamer (C) and nonamer (D) in (A).

E Fourier shell correlation (FSC) curves of the final cryo-EM maps of hexamer (blue line), heptamer (black line) and nonamer (red line), using the gold standard FSC 0.143 criteria.

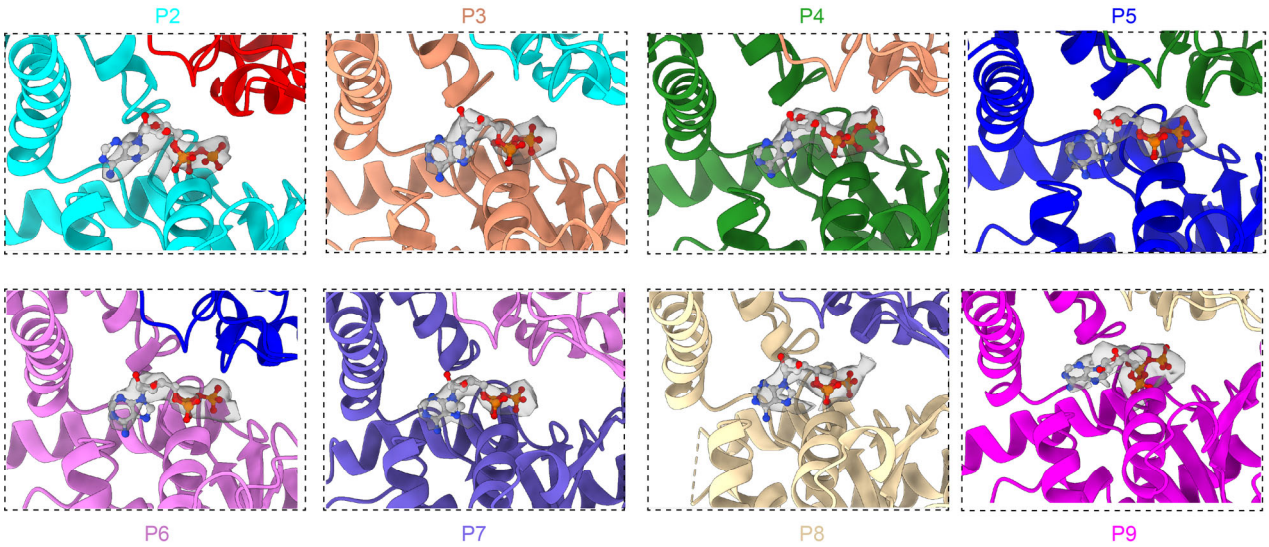

S11. Nucleotide binding states of the nine ATPase sites in the nonamer.

ATP occupation of all the ATPase sites in the nonamer. The atomic models are color-coded for different protomers. The segmented density maps of ATP were superimposed with the atomic model.

904 **S1 Table. Cryo-EM data collection, refinement and validation statistics**

	CLPB	$CLPB^{E425Q}$	NBD^{E425Q}		
			Hexamer	Hetamer	Nonamer
EMDB/PDB	33105	33106	33109	33110	33104/7XBK
Data collection and processing					
Microscope and camera	Titan Krios K3	Titan Krios K2	Titan Krios G3i, K3		
Magnification	81,000	36,000	64,000		
Voltage (kV)	300	300	300		
Electron exposure (e^-/Å^2)	60	58	50		
Pixel size (Å)	1.07	1.052	1.08		
Map resolution (Å)	6.8	7.9	7.4	4.1	3.7
FSC threshold	0.143				
Map resolution range (Å)	4-7	5-9	4-8	4-8	3.5-7
Refinement					
Map sharpening B factor (Å^2)	-89.9	-155.0	-237.2	-83.4	-97.3
Model composition					
Non-hydrogen atoms	-	-	-	-	25745
Protein residues	-	-	-	-	3156
Ligands	-	-	-	-	8 Mg+8ATP
B factors (Å^2)					
Protein	-	-	-	-	88.42
Ligand	-	-	-	-	66.90
R.m.s. deviations					
Bond lengths (Å)	-	-	-	-	0.005
Bond angles (°)	-	-	-	-	0.863
Validation					
MolProbity score	-	-	-	-	1.48
Clash score	-	-	-	-	5.67
Ramachandran plot					
Favored (%)	-	-	-	-	97.04
Allowed (%)	-	-	-	-	2.93

S2 Table. Data collection and refinement statistics of the CLPB_ANK

	CLPB_ANK
Data collection[a]	
Space group	C121
Cell dimensions	
a, *b*, *c* (Å)	30.31 67.68 84.98
α, β, γ	90.0 96.05 90.00
Resolution (Å)	33.84-1.99 (2.04-1.99)[b]
R_{merge}	0.058 (0.623)
R_{meas}	0.070 (0.739)
$I / \sigma I$	11.2 (1.9)
CC(1/2)	0.998 (0.865)
Completeness (%)	99.4 (99.5)
Redundancy	1.6 (1.7)
Refinement	
Resolution (Å)	2.1
No. reflections	9,966
R_{work}/R_{free} (%)	20.6/23.6
No. atoms	
Protein	1,287
Water	29
B-factors (Å^2)	
Protein	49.0
Water	43.9
R.m.s. deviations	
Bond lengths (Å)	0.003
Bond angles (°)	0.629
Ramachandran stat.(%)	98.78 / 1.22 / 0.0 / 0.0[c]

[a] One crystal was used for data collection.

[b] Values in parentheses are for the highest-resolution shell.

[c] Values are in percentage and are for most favoured, additionally allowed, generously allowed, and disallowed regions in Ramachandran plots, respectively.